Supporting Information

Thermochromic uranyl isothiocyanates: Influencing charge transfer bands with supramolecular structure.

Robert G. Surbella III[1], Lucas C. Ducati[2], Jochen Autschbach[3], Nicholas P. Deifel[4] and Christopher L. Cahill[1*]

[1]Department of Chemistry, The George Washington University, 800 22nd St N.W., Washington, D.C. 20052.

[2]Department of Fundamental Chemistry Institute of Chemistry, University of São Paulo, Av. Prof. Lineu Prestes 748, São Paulo, SP 05508-000, Brazil.

[3]Department of Chemistry, University at Buffalo, State University of New York, 312 Natural Sciences Complex, Buffalo, New York 14260.

[4]Department of Chemistry, Hampden-Sydney College, Hampden-Sydney, VA 23943.

Table of Contents

1. Synthetic Details:

*A Typical Synthetic Procedure for **1** - **7***:

Uranyl nitrate hexahydrate (UNH - 0.100g, 0.249mmol) was dissolved in 5mL of acetone and stirred in the presence of potassium thiocyanate (KSCN - 0.137g, 1.49mmol) for roughly 12 hours. A white crystalline solid (KNO_3) precipitated from the bright yellow solution and was discarded. The solution was heated and stirred until most of the solvent had evaporated and an orange or yellow solid remained. The solid was dissolved in DI H_2O and stirred until a clear yellow solution persisted. Three molar equivalents of the appropriate pyridine were added to the solution. The solution was stirred, gently heated and acidified with 3M HCl. Once the organic was completely dissolved, the solution was cooled, covered with perforated parafilm and left to evaporate under ambient conditions.

*Notes on the Synthesis of **1** and **3**:*

Compounds **1**, $(C_{10}H_{10}N)_3[UO_2(NCS)_5] \cdot 3H_2O$, and **3**, $(C_{10}H_{10}N)_3[UO_2(NCS)_5]$, can be prepared directly and isolated as pure phases, yet **1** (post synthesis) is prone to dehydration and subsequently rearranges to form **3**. The differences in the synthetic parameters that promote the formation of **1** vs. **3** are subtle and often overlap. The optimal conditions for promoting single crystal growth of **1** and **3** are provided in Table S1. Fluctuations in laboratory temperature due to seasonal changes seem to influence product formation, yet a quantitative correlation between temperature and product distribution could not be established.

Table S1. Optimal synthetic parameters for the formation of **1** and **2**.

	1. $(C_{10}H_{10}N)_3[UO_2(NCS)_5] \cdot 3H_2O$	**2**. $(C_{10}H_{10}N)_3[UO_2(NCS)_5]$
UNH	0.249 mmol	0.249 mmol
KSCN	1.49 mmol	2.98 mmol
4-PP	0.747 mmol	0.747 mmol
H_2O	7-8 mL	10 mL
pH*	0.65 –1.20	1.20 – 1.40

***** Adjusted with 3M HCl.

*Notes on the Synthesis of **3** - **7**:*

The initial pH and concentration of [SCN^-] influences the relative product distribution of **3** - **7**. The synthetic parameters provided in Tables S2 and S3 should be interpreted as guidelines to increase the likelihood of forming each phase **3** - **7**. Preparing pure phases is difficult and co-crystallization is the norm. The low solubility of 4,4'-dipyridyl necessitates the ligand to water ratio be scaled accordingly. Note the role of temperature was not investigated in the synthesis of **3** - **7**.

Table S2. Optimal synthetic parameters for the preparation of **3** - **5**.

	3: $(C_{10}H_9N_2)_3[UO_2(NCS)_5]$	**4:** $(C_{10}H_{10}N_2)_{1.5}[UO_2(NCS)_5] \cdot 2H_2O$	**5:** $(C_{10}H_{10}N_2)_2[UO_2(NCS)_{4.75}Cl_{0.25}] \cdot SCN$
UNH	0.249 mmol	0.249mmol	0.249 mmol
KSCN	1.49 mmol	1.49 mmol	1.49 mmol
4,4'-BIPY	0.747 mmol	0.747 mmol	0.747 mmol
H_2O	8-10 mL	8-10 mL	8-10 mL
pH*	1.50 – 3.50	0.75 – 2.00	0.75 – 1.50

*Adjusted with 3M HCl

*Notes specific to the synthesis of **3**: $(C_{10}H_9N_2)_3[UO_2(NCS)_5]$*

Compound **3** is the most frequently observed phase as it forms over a wide pH range: 0.8 – 3.5. Syntheses of **3** performed between the pH range of 1.50 – 3.50 results in maximum yields whereas the pH range of 3.0 – 3.5 will typically produce a pure phase. All syntheses performed at or below pH 3.0 generally lead to co-crystallization of **3** with **4**. Lower pH values < 1.3 and/or allowing the mother liquor to approach or reach dryness typically leads to a mixture of **3** - **5** and **7** as determined by optical inspection and manual separation of the crystalline phases followed by PXRD.

*Notes specific to the synthesis of **4**:* $(C_{10}H_{10}N_2)_{1.5}[UO_2(NCS)_5] \cdot 2\ H_2O$

Compound **4** is the second most frequently observed species and has a maximum yield over the pH range of 1.3 – 1.5. The crystallization of **4** typically occurs over the course of several weeks, yet prior to complete evaporation of the mother liquor. At or near dryness of the reaction media, compounds **5** - **7** co-crystalize with **4** and their respective product distributions appear to be influenced by the initial reaction pH and concentrations of: [Cl^-], [NCS^-] and [UO_2^{2+}]. Note this observation is only semi-quantitative at best and based upon optical inspection of the post synthetic product distributions.

*Notes specific to the synthesis of **5**, $(C_{10}H_{10}N_2)_2[UO_2(NCS)_{4.75}Cl_{0.25}] \cdot SCN$, and **6**, $(C_{10}H_{10}N_2)_2[UO_2(NCS)_5] \cdot NO_3$*

Compounds **5** and **6** were never synthesized as pure phases and formed only as part of co-crystallizations. The incorporation of one anion (NO_3^- vs. NCS^-) into the structures of **5** and **6** are seemingly influenced by the initial [SCN^-] concentration. A six-fold excess of potassium thiocyanate (compared to UNH) favors the formation **5**, whereas a twelve-fold excess favors the production of **6**.

These phases tend to form as the mother liquor approaches dryness and after the formation of **3** and/or **4**. We can thus speculate appreciable competition for ligand coordination to the remaining [UO_2^{2+}] in solution exists as a function of depletion in the initial [SCN^-] and an enrichment in [Cl^-] concentration. This may explain the partial substitution of an isothiocyanate for that of a chloro ligand in **5**, whereas no

substitution is observed when higher initial [SCN^-] concentrations are utilized in **6**. The incomplete precipitation of nitrate during synthesis is likely responsible for the incorporation of the NO_3^- anions in **6**.

Table S3. Optimal synthetic parameters for the preparation of **6** - **7**.

	6: **$(C_{10}H_9N_2)_3[UO_2(NCS)_5] \cdot NO_3$**	**7:** **$(C_{10}H_{10}N_2)_2[UO_2(NCS)_4Cl] \cdot Cl \cdot 2H_2O$**
UNH	0.249 mmol	0.249 mmol
KSCN	2.51 mmol	0.996 - 1.49 mmol
4,4'-BIPY	0.747 mmol	0.747 mmol
H_2O	8-10 mL	8-10 mL
pH*	0.75 – 1.50	0.50 – 1.25

*Adjusted with 3M HCl

*Notes specific to the synthesis of **7**, $(C_{10}H_{10}N_2)_2[UO_2(NCS)_4Cl] \cdot Cl \cdot 2H_2O$*

Compound **7** typically co-crystallizes with **4**, with the latter forming first. The depletion of [SCN^-] in the reaction media, due to the formation of **4**, combined with the already lower initial concentration of [SCN^-] used (compared to **5** and **6** – **Tables S2** and **S3**) likely contributes to the substitution of a chloro ligand in place of an isothiocyanate in the structure of **7**. The lower initial pH value (compared to **5** and **6**) likely provided a [Cl^-] high enough to lead to the incorporation of a chloride anion and chloro ligand in **7**.

2. The Phase Transformation of 1 to 2

Crystals or powder samples of compound **1**, $(C_{11}H_{10}N_3)_3[UO_2(NCS)_5] \cdot 3H_2O$, are unstable outside of the mother liquor and are susceptible to dehydration and subsequent rearrangement to yield compound **2**. The transformation of **1** → **2** was monitored and studied via optical microscopy, powder and single crystal X-ray diffraction, the findings of each are described below. We note that large single

crystals of **2** can be prepared directly and are stable outside of their mother liquor as no phase transitions or degradation have been observed.

Monitoring the phase transformation: Optical Microscopy and PXRD

Compound **1** is bright orange in color whereas compound **2** is bright yellow, these two phases can therefore be easily distinguished visually (**Photo S1**). A batch of orange crystals (of **1**) was prepared and a portion of which was removed from the mother liquor and placed on a glass microscope slide and monitored via 10x optical microscopy. The crystals changed from bright orange to opaque and yellow (**Photo S2**). The opaque yellow crystals were analyzed via PXRD and determined to be purely composed of compound **2**.

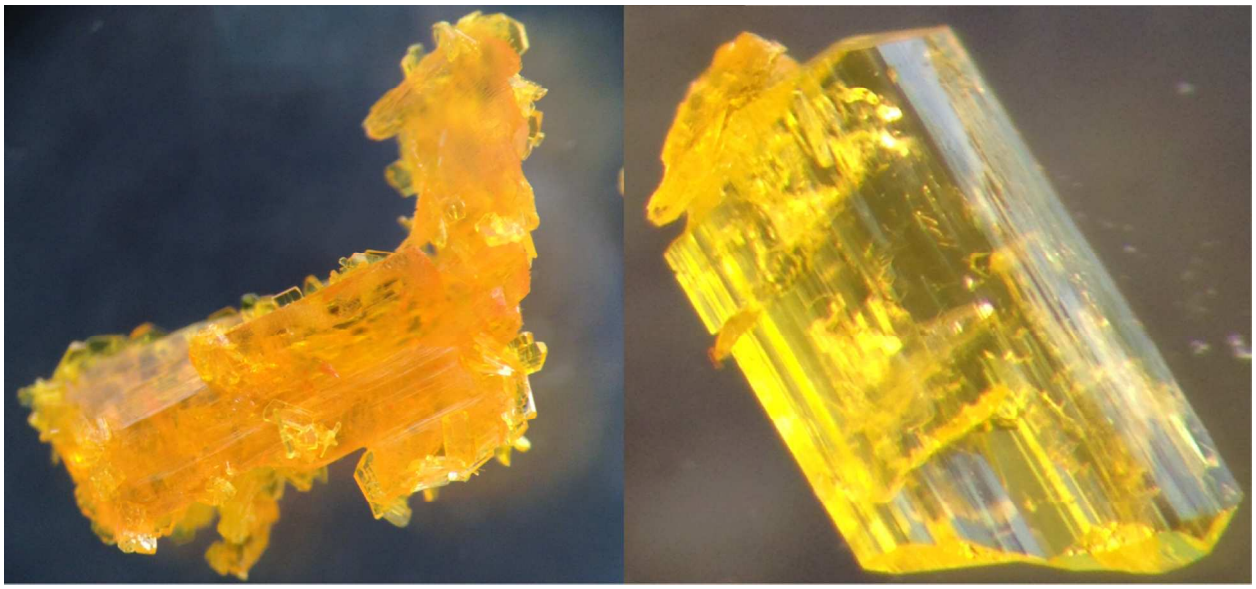

Photo S1. The crystals of **1** (left) are orange whereas those of **2** (right) are yellow.

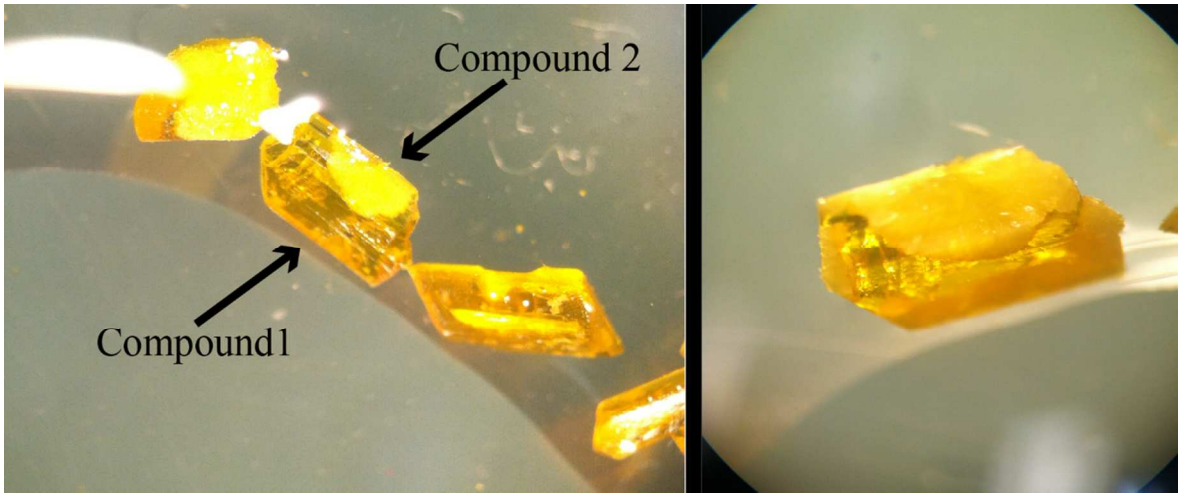

Photo S2. Left: Several orange crystals of **1** are in transition to yield **2,** which is opaque and yellow. Right: An expanded view of a single crystal of **1** that is mid-transition to **2**.

Monitoring the phase transformation: Single Crystal and Powder X-ray Diffraction

An orange single crystal of **1** was isolated from the mother liquor and reflection data were collected to unit cell parameters determine: a = 9.5941(8) Å, b = 14.336(1) Å, c = 16.243(1) Å, α = 94.758(1)°, β = 101.843(1)°, γ = 97.901(1)°. This crystal was then lightly crushed onto the center of a PXRD sample holder and allowed to sit in air for several minutes. After which, PXRD diffraction data were collected and the peak positions and intensities corresponded with that of compound **2** (**Figure S1**). PXRD analysis was performed as several attempts to first capture this transition on a single crystal were unsuccessful. The stress of the dehydration and subsequent rearrangement resulted in a polycrystalline sample. The loss in crystallinity is however, not instantaneous and as such, we captured the structure of **1M**. The structure of **1M**, **(**$C_{10}H_{11}N)_3[UO_2(NCS)_5]$, is an intermediate between **1** and **2** and contains structural sentiments of both **1** and **2** (**Figure S2**).

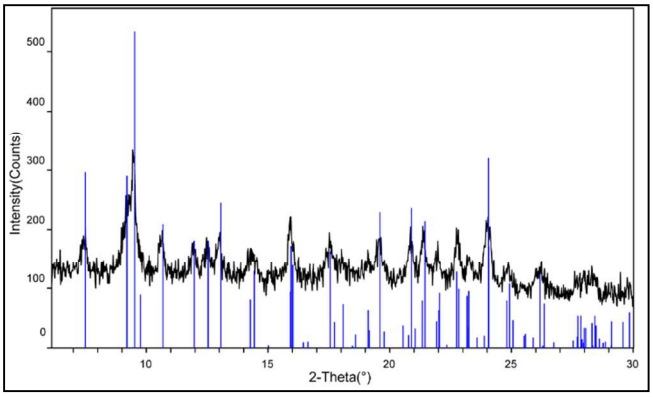

Figure S1. The observed powder X-ray diffraction pattern of a crushed single crystal of **1** post transformation with the calculated pattern of **2** overlaid in blue.

The data collection of 1M.

A large crystal (500 μm) of **1** was cooled to 285K under a N_2 gas stream while reflection data were collected. The unit cell parameters of the crystal were determined in 10 minute intervals until the cell parameters no longer corresponded to **1**. The crystal was immediately cooled to 100(2)K and a full data set was collected, details are provided in Table S4. The stress caused by this transformation resulted in a gradual loss in crystallinity and as such, the final refinement contained several issues: most notably, regions of residual electron density, large ADP min/max rations and a failure of the refinement to converge. We are however, confident in the structural determination as the R values (R_1 12.75% wR_2 - 25.13%) suggest a structurally correct model. Several of the 4-phenylpyridinium cations and isothiocyanate ligands in **2** were positionally disordered and required the use of PART instructions and individual atoms (e.g. C, N and S) required ISOR restraints. The U-N bond distances on U2 were restrained at 2.43Å (DFIX) and refined using a free variable.

Compound 1M: $(C_{10}H_{10}N)_3[UO_2(NCS)_5]$

The $[UO_2(NCS)_5]^{3-}$ tectons form two distinct pairs, the first of which is formed by way of S···S interactions and are akin to those pairs observed in **1** whereas the second are formed via S···O interactions (**Figure S3** and **Table S5**). The S···O interactions are much longer than the sum of the van der Waal radii

for S and O (at 120% vdW), yet are of note as these interactions *are* prominent in **2** and are therefore being observed prior to their formation (**Figure S2**). These two distinct types of $[UO_2(NCS)_5]^{3-}$ tecton pairs alternate and are linked to one another via S···S interactions, giving rise to chains that arrange parallel to one another and ultimately form an anionic layers in the (0-11) plane. The 4-PPH cations form columns via offset π-interactions, yet are disjointed as several of the cations are regularly displaced or contorted out-of-plane, disrupting the cationic stacking motif observed in **1 (Figure S4)**. The 4-PPH cations form several N-H···S hydrogen bonds to the uranyl tectons, relevant interaction distances and angles of which are provided in **Table S5**.

Table S4. Selected crystallographic parameters of 1M.

Compound	**1M**
Formula	$(C_{11}H_{10}N)_3[UO_2(NCS)_5]$
Formula mass	1029.03
Crystal Size mm^3	0.552 x 0.500 x 0.297
Crystal Color	Light Orange
Crystal system	Triclinic
Space group	$P\,1^{-}$
Z	4
Radiation type	Mo Kα
Temperature/K	100(2)
a (Å)	9.569(2)
b (Å)	16.751(4)
c (Å)	26.791(7)
α (°)	97.899(4)
β (°)	92.222(3)
γ (°)	103.332(3)
Unit cell volume ($Å^3$)	4128.0(2)
Dcalc/Mg m^{-3}	1.656
Absorption coefficient, μ/mm^{-1}	4.229
No. of measured reflections	56501
No. of independent reflections	22363
Rint	0.0594
Final R1 values ($I > 2\sigma(I)$)	0.1275
Final wR2 (F2) values ($I > 2\sigma(I)$)	0.2513
Final R1 values (all data)	0.1500
Final wR2(F2) values (all data)	0.2584
Goodness of fit on F^2	1.375
CSD Number	1567368

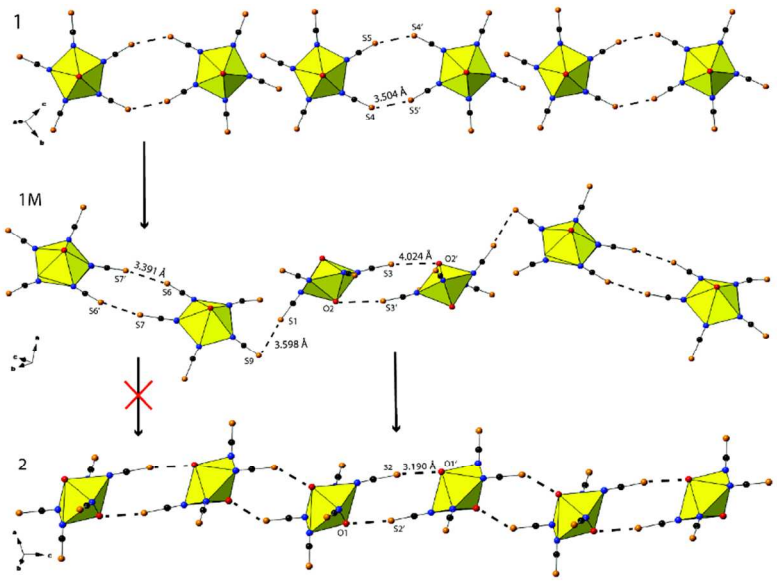

Figure S2. The black arrows highlight the structural elements present in **1M** (middle) that are common to both **1** (top) and **2** (bottom).

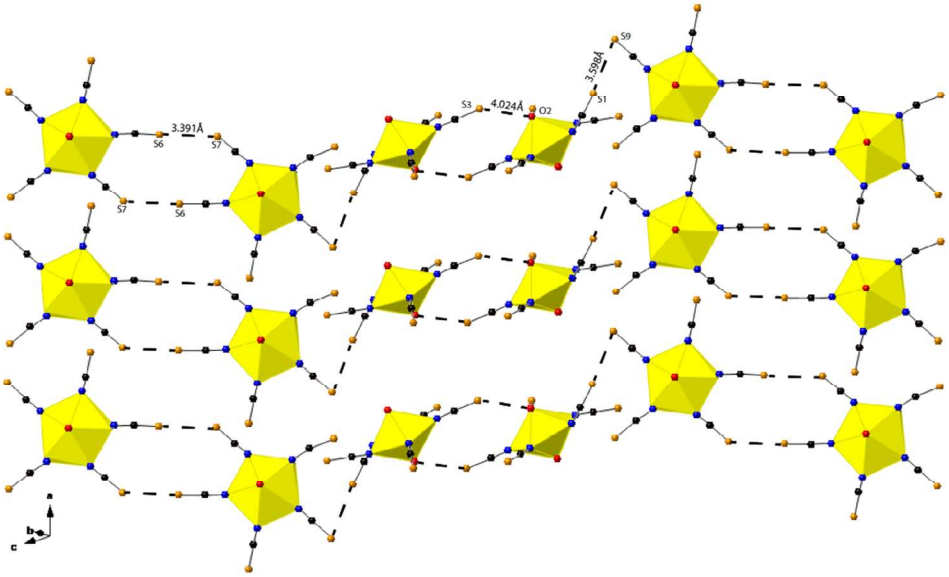

Figure S3. Pairs of $[UO_2(NCS)_5]^{3-}$ tectons in **1M** are linked into chains along the [011] direction via S···S and S···O interactions. The chains arrange in a parallel fashion to form sheets in (0-11).

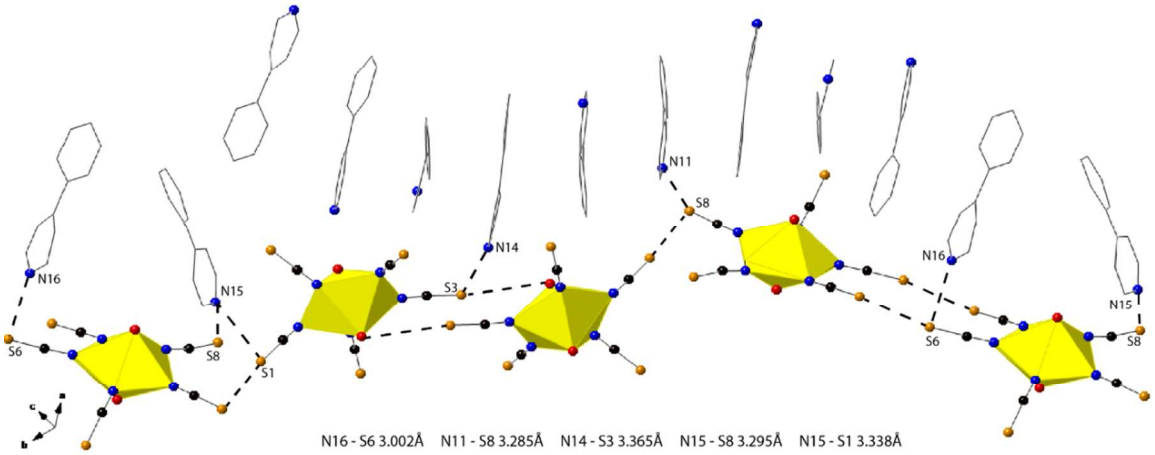

Figure S4. The cationic stacking motif in **1M**. All H atoms have been omitted here and throughout the supporting information for clarity.

Table S5. Selected non-covalent interaction distances and angles in **1M**.

Interaction	Distance (Å)	Angle (°)
N_{11}-H_{n11}···S_9	3.28(2)	∠C_9-S_9-N_{11} - 91.2(6)
N_{12}-H_{n12}···O_1	3.00(2)	∠U_1-O_1-N_{12} - 117.7(6)
N_{13}-H_{n13}···S_{10}	3.25(2)	∠C_{10}-S_{10}-N_{13} - 90.4(7)
N_{14}-H_{n14}···S_3	3.37(2)	∠C_3-S_3-N_{14} - 93.6(6)
N_{15a}-H_{n15a}···S_1	3.35(3)	∠C_1-S_1-N_{15} - 89.2(9)
N_{15a}-H_{n15a}···S_8	3.28(6)	∠C_8-S_8-N_{15a} - 62(1)
N_{16a}-H_{n16a}···S_6	3.4(1)	∠C_{6a}-S_{6a}-N_{16a} - 85(4)
S_6···S_7	3.39(5)	C_6-S_6···S_7 -171(4)
S_3···O_2	4.03(1)	C_3-S_3···O_2 -140.6(6)
S_1···S_9	3.599(8)	C_1-S_1···S_9 -174.2(6)

3. Single Crystal X-Ray diffraction data of 1 – 7 at 100(2)K.

Single crystals of **1 – 7** were mounted on MicroMounts (Mitegen) and reflection data were collected using 0.5°ω scans at 100(2)K on a Bruker SMART diffractometer equipped with an APEX II CCD detector with a Mo Kα source (**Table 1**, of the main manuscript). The APEX II software suite[1] was used to integrate the data and apply an absorption correction (SADABS).[2] The structures were solved using direct methods via SHELXS[3] and refined using SHELXL-15[4] within the WINGX software suite.[5]

Publication materials were prepared using EnCifer[6] whereas figures of the title compounds were made using CrystalMaker v9.1.4.[7]

All of the non-hydrogen atoms in **1-7** were located using difference Fourier maps and refined anisotropically. The hydrogen atoms located on the carbon atoms of the pyridinium cations were placed in idealized positions and allowed to ride on their parent atoms. The hydrogen atoms associated with the nitrogen atom on each pyridinium cation **1** – **7** were located in difference Fourier maps, modeled, restrained (DFIX) and refined isotropically. The hydrogen atoms associated with the water molecules in **1** were located in the difference Fourier maps and modeled using DIFX (0.84 and 0.01) and DANG (1.32 and 0.04) restraints. There are two unique water molecules (Ow1 and Ow2) in **4**, one of which (Ow1) was disordered over two positions and required the use of a PART command. The hydrogen atoms associated with both parts (Ow1a and Ow1b) could not be located in the difference Fourier maps and were not modeled. The hydrogen atoms associated with Ow2 were located in the difference Fourier map and modeled using DFIX (0.84 and 0.01) and DANG (1.32 and 0.04) restraints.

An equatorial ligand site in **5** is partially occupied by an isothiocyanate (75%) and chloro (25%) ligand and required the use of a PART instruction. The resulting U-N (2.34(1) Å - Avg. of other U-N distances 2.433 Å) and U-Cl (2.980(9) Å) bond lengths are shorter and longer, respectively, than expected, yet were not deemed egregious and were therefore not distance restrained.

The crystal used in the data collection of **7** was twinned and treated using Cell_Now.[8] Two non-merohedral twin domains (~90:10) were found and are related by a 179.8° rotation about [100]. The reflection data were integrated using SAINT[9] and an absorption correction was applied using TWINABS.[10] Compound **7** contains two crystallographically unique solvent water molecules (Ow1 and Ow2) and although the hydrogen atoms associated with them were located in the difference Fourier maps, only those belonging to Ow1 could be modeled and required DIFX (0.84 and 0.01) and DANG (1.32 and 0.04) restraints.

4. Single Crystal X-Ray diffraction data of 1 – 7RT at 296(2)K.

Single crystals of **1 – 7** were mounted on MicroMounts (Mitegen) and reflection data were collected using 0.5°ω scans at 296(2)K (note **1** was collected at 285(2)K) on a Bruker SMART diffractometer equipped with an APEX II CCD detector with a Mo Kα source (**Table S6)**. The APEX II software suite[1] was used to integrate the data and apply an absorption correction (SADABS).[2] The structures were solved using direct methods via SHELXS[3] and refined using SHELXL-15[4] within the WINGX software suite.[5] Publication materials were prepared using EnCifer[6] whereas figures of the title compounds were made using CrystalMaker v9.1.4.[7]

All of the non-hydrogen atoms in **1RT - 7RT** were located using difference Fourier maps and refined anisotropically. The hydrogen atoms located on the carbon and nitrogen atoms of the pyridinium cations were placed in idealized positions and allowed to ride on their parent atoms.

The hydrogen atoms associated with the three unique water molecules in **1RT** were able to be located in the difference Fourier maps, yet were unable to be modeled and refined. There are two unique water molecules (Ow1 and Ow2) in **4RT**, one of which (Ow1) was disordered over two positions and required the use of a PART command. The hydrogen atoms associated with both parts (Ow1a and Ow1b) could not be located in the difference Fourier maps and were not modeled. The hydrogen atoms associated with Ow2 were located in the difference Fourier map and modeled using DFIX (0.84 and 0.01) and DANG (1.32 and 0.04) restraints. The hydrogen atoms associated with the water molecule (Ow1) in **7RT** were modeled, yet required the use of DIFX (0.84 and 0.01) and DANG (1.32 and 0.04) restraints.

Crystals of **1RT** are prone to phase transformation (i.e. dehydration followed by a structural rearrangement to yield **2RT**) and as such, the highest temperature a full X-ray diffraction experiment could be conducted was 285(2)K; the crystal of **1RT** ultimately underwent a phase transformation during the end of the data collection.

An S atom (S1) in **2RT** was positionally disordered and required the use of a PART instruction. An equatorial ligand site in **5RT** is partially occupied by an isothiocyanate (75%) and chloro (25%)

ligand and required the use of a PART instruction. The resulting U-N (2.34(1) Å - Avg. of other U-N distances 2.433 Å) and U-Cl (2.980(9) Å) bond lengths are shorter and longer, respectively, than expected yet were not deemed egregious and were not distance restrained.

The crystal used in the data collection of **7RT** was twinned and treated using Cell_Now.[8] Two non-merohedral twin domains (~90:10) were found and are related by a 179.8° rotation about [100]. The reflection data were integrated using SAINT[9] and an absorption correction was applied using TWINABS.[10] Compound **7RT** contains two crystallographically unique solvent water molecules (Ow1 and Ow2) and although the hydrogen atoms associated with them were located in the difference Fourier maps, only those belonging to Ow1 could be modeled and required DIFX (0.84 and 0.01) and DANG (1.32 and 0.04) restraints.

Table S6. Selected crystallographic data pertaining to the 296K data collections of **1 - 7**.

Compound	**1RT**	**2RT**	**3RT**
Formula	$(C_{11}H_{10}N)_3$ $[UO_2(NCS)_5]$ $\cdot 3H_2O$	$(C_{11}H_{10}N)_3[UO_2(NCS)_5]$	$(C_{10}H_9N_2)_3[UO_2(NCS)_5]$
Formula mass	1077.03	1029.03	1035.02
Crystal Size mm3	0.200 x 0.150 x 0.100	0.277 x 0.217 x 0.191	0.255 x 0.231 x 0.093
Crystal Color	Orange	Yellow	Red
Crystal system	Triclinic	Monoclinic	Orthorhombic
Space group	*P-1*	*C2/c*	*Cmca*
Z	2	4	8
Radiation type	Mo Kα	Mo Kα	Mo Kα
Temperature/K	285(2)	296(2)	296(2)
a (Å)	9.6370(18)	10.4405(4)	17.350(11)
b (Å)	14.392(3)	23.5757(8)	19.615(13)
c (Å)	16.487(3)	17.1232(6)	23.359(15)
α (°)	93.623(3)°	90	90
β (°)	102.183(3)°	104.79	90
γ (°)	96.820(3)°	90	90
Unit cell volume ($Å^3$)	2210.2(7)	4075.1(3)	7950(9)
Dcalc/Mg m^{-3}	1.618	1.677	1.730
Absorption coefficient, μ/mm-1	3.957	4.283	4.394
No. of measured reflections	22355	21885	24112
No. of independent reflections	11053	5457	4482
Rint	0.0458	0.0215	0.0496
Final R1 values (I > 2σ(I))	0.0447	0.0186	0.0263
Final wR2 (F2) values (I > 2σ(I))	0.1067	0.0421	0.0505
Final R1 values (all data)	0.0626	0.0221	0.0426
Final wR2(F2) values (all data)	0.1137	0.0432	0.0554
Goodness of fit on F^2	1.045	1.043	0.995
CSD Number	1567354	1567355	1567356

Compound	**4RT**	**5RT**	**6RT**
Formula	$(C_{10}H_{10}N_2)_{1.5}$ $[UO_2(NCS)_5]\cdot 2H_2O$	$(C_{10}H_{10}N_2)_2$ $[UO_2(NCS)_{4.75}Cl_{0.25}]\cdot SCN$	$(C_{10}H_{10}N_2)_2$ $[UO_2(NCS)_5]\cdot NO_3$
Formula mass	831.74	929.59	938.84
Crystal Size mm^3	0.490 x 0.392 x 0.343	0.294 x 0.248 x 0.207	0.538 x 0.248 x 0.195
Crystal Color	Orange	Dark Orange	Yellow
Crystal system	Monoclinic	Orthorhombic	Orthorhombic
Space group	*C2/c*	*Pnma*	*Pnma*
Z	8	4	4
Radiation type	Mo Kα	Mo Kα	Mo Kα
Temperature/K	296(2)	296(2)	296(2)
a (Å)	22.9446(18)	14.7865(5)	14.3739(11)
b (Å)	12.8805(10)	23.3593(7)	23.6011(18)
c (Å)	21.3121(17)	9.7127(3)	9.8045(8)
α (°)	90	90	90
β (°)	113.7400(10)	90	90
γ (°)	90	90	90
Unit cell volume ($Å^3$)	5765.6(8)	3354.79(18)	3326.1(5)
Dcalc/Mg m^{-3}	1.916	1.841	1.875
Absorption coefficient, μ/mm^{-1}	6.034	5.257	5.246
No. of measured reflections	42274	38952	38434
No. of independent reflections	8293	3533	3493
Rint	0.0315	0.0270	0.0327
Final R1 values ($I > 2\sigma(I)$)	0.0253	0.0425	0.0458
Final wR2 (F2) values ($I > 2\sigma(I)$)	0.0563	0.0932	0.1001
Final R1 values (all data)	0.0357	0.0462	0.0481
Final wR2(F2) values (all data)	0.0593	0.0945	0.1009
Goodness of fit on F^2	1.017	1.229	1.306
CSD Number	1567357	1567358	1567359

Compound	**7RT**

Formula	$(C_{10}H_{10}N_2)_2[UO_2(NCS)_5] \cdot Cl \cdot H_2O$
Formula mass	907.66
Crystal Size mm^3	0.204 x 0.094 x 0.066
Crystal Color	Light Yellow
Crystal system	Orthorhombic
Space group	Pnma
Z	4
Radiation type	Mo Kα
Temperature/K	296(2)
a (Å)	14.0607(16)
b (Å)	22.900(3)
c (Å)	9.9560(11)
α (°)	90
β (°)	90
γ (°)	90
Unit cell volume ($Å^3$)	3205.7(7)
Dcalc/Mg m^{-3}	1.881
Absorption coefficient, μ/mm^{-1}	5.531
No. of measured reflections	27160
No. of independent reflections	3454
Rint	0.1336
Final R1 values ($I > 2\sigma(I)$)	0.0461
Final wR2 (F2) values ($I > 2\sigma(I)$)	0.0856
Final R1 values (all data)	0.0580
Final wR2(F2) values (all data)	0.0883
Goodness of fit on F^2	1.270
CSD Number	1567360

5. Bond lengths, angles and non-covalent interaction distances from 1 - 7.

Table S7. Sulfur based linkage distances from the structures of **1** - **7** at 100K and 296K.

Compound	Interaction	Distance (Å)	Angle (°)	
1 – 100K	2x $S_4\cdots S_5$	3.504(1)	C_4-$S_4\cdots S_5$	150.17(12)
1 – 296K	2x $S_5\cdots S_4$	3.584(3)	C_5-S_5-S_4	153.0(2)
2 – 100K	$S_2\cdots O_{yl}$	3.1904(14)	C_2-$S_2\cdots O_{yl}$	148.64(6)
2 – 296K	$S_2\cdots O_{yl}$	3.2986(16)	C_2-$S_2\cdots O_{yl}$	147.93(8)
3 – 100K	$S_3\cdots S_4$	3.3510(10)	C_3-$S_3\cdots S_4$	149.29(13)
	$S_5\cdots C_4(\pi)S_4$	3.385	C_5-$S_5\cdots C_4(\pi)S_4$	168.8
3 – 296K	$S_3\cdots S_4$	3.448(3)	C_3-$S_3\cdots S_4$	147.3(2)
	$S_5\cdots C_4(\pi)S_4$	3.494	C_5-$S_5\cdots C_4(\pi)S_4$	165.6
4 – 100K	$S_4\cdots S_{4'}$	3.3123(9)	C_2-$S_2\cdots S_{4'}$	164.7(1)
	$S_2\cdots S_5$	3.3163(6)	C_2-$S_2\cdots S_5$	164.65(8)
	$S_5\cdots S_2$	3.3163(6)	C_5-$S_5\cdots S_2$	127.95(7)
4 – 296K	$S_2\cdots S_2'$	3.4172(11)	C_2-$S_2\cdots S_2'$	163.71(15)
	$S_3\cdots S_5$	3.3787(12)	C_3-$S_3\cdots S_5$	127.47(10)
	$S_5\cdots S_3$	3.3787(12)	C_5-$S_5\cdots S_3$	163.12(12)
5 – 100K	4x $S_1\cdots S_2$	3.319(3)	C_1-$S_1\cdots S_2$	178.4(3)
5 – 296K	4x $S_1\cdots S_2$	3.349(3)	C_1-$S_1\cdots S_2$	176.9(2)
6 – 100K	4x $S_1\cdots S_2$	3.3414(19)	C_1-$S_1\cdots S_2$	179.15(16)
6 – 296K	4x $S_2\cdots S_3$	3.380(3)	C_2-$S_2\cdots S_3$	176.3(3)
7 – 100K	4x $S_1\cdots S_2$	3.236(2)	C_1-$S_1\cdots S_2$	173.82(18)
7 – 296K	4x $S_1\cdots S_2$	3.285(3)	C_1-$S_1\cdots S_2$	173.4(2)

Table S8. Selected bond angles of the $[UO_2(NCS)_5]^{3-}$ and $[UO_2(NCS)_4Cl]^{3-}$ tectons across **1** - **7**.

1		**2**		**3**		**4**	
O1-U-N1	88.50(10)	O1-U-N1	89.19(3)	O1-U-N1	90.14(5)	O1-U-N1	91.03(8)
O1-U-N2	90.64(10)	O1-U-N2	88.52(6)	O1-U-N2	90.11(5)	O1-U-N2	87.02(7)
O1-U-N3	86.75(10)	O1-U-N3	92.41(5)	O1-U-N3	89.93(5)	O1-U-N3	93.05(7)
O1-U-N4	90.92(10)	N1-U-N2	73.15(3)	O1-U-N4	89.85(5)	O1-U-N4	87.85(7)
O1-U-N5	92.41(10)	N2-U-N3	71.99(5)	O1-U-N5	89.98(5)	O1-U-N5	88.84(7)
N1-U-N2	74.90(9)	N3-U-N3’	69.90(5)	N1-U-N2	72.54(11)	N1-U-N2	69.74(7)
N2-U-N3	72.03(9)			N2-U-N3	71.96(11)	N2-U-N3	71.28(6)
N3-U-N4	71.01(9)			N3-U-N4	71.73(10)	N3-U-N4	72.91(7)
N4-U-N5	69.59(9)			N4-U-N5	73.62(10)	N4-U-N5	72.62(7)
N5-U-N1	72.73(9)			N5-U-N1	70.15(10)	N5-U-N1	73.92(7)

5		**6**		**7**	
O1-U-N1	91.61(19)	O1-U-N1	90.69(14)	O1-U-N1	92.19(15)
O1-U-N2	90.50(14)	O1-U-N2	89.2(2)	O1-U-N2	90.64(16)
O1-U-N3	90.3(3)	O1-U-N3	89.47(17)	O1-U-N3	88.47(17)
N1-U-N2	71.02(16)	N1-U-N2	71.55(12)	O1-U-N4	87.38(16)
N2-U-N3	71.90(12)	N1-U-N3	71.32(16)	O1-U-Cl1	91.36(14)
				Cl1-U-N1	71.86(10)
				N1-U-N2	71.44(14)
				N2-U-N3	71.50(15)
				N3-U-N4	70.94(15)
				N4-U-Cl1	74.28(11)

Table S9. Selected non-covalent interaction distances in **1,** $(C_{11}H_{10}N)_3[UO_2(NCS)_5] \cdot 3H_2O$, as measured at 100K.

Interaction	Distance (Å)	Perpendicular Distance	Distance (Å)	Angle Beta (°)
$Ow_1 \cdots Ow_2$	2.766(4)	-	-	
$Ow_1 \cdots Ow_3$	2.733(4)	-	-	
$Ow_2 \cdots Ow_3$	2.857(4)	-	-	
$Cg_1 \cdots Cg_2$	3.659(2)	$Cg_1 \cdots Cg_2 \perp$	3.448(1)	27.0
$Cg_1 \cdots Cg_4$	3.584(2)	$Cg_1 \cdots Cg_4 \perp$	3.454(1)	15.5
$Cg_3 \cdots Cg_6$	3.720(2)	$Cg_3 \cdots Cg_6 \perp$	3.368(1)	16.6
$Cg_4 \cdots Cg_5$	3.572(2)	$Cg_4 \cdots Cg_5 \perp$	3.491(2)	9.8
$Cg_5 \cdots Cg_6$	3.820(2)	$Cg_5 \cdots Cg_6 \perp$	3.343(1)	16.6

Cg refers to the center of gravity of an aromatic ring.

Cg1 (N_6 and C_6-C_{10}). Cg2 (C_{11}-C_{16}). Cg3 (N_7 and C_{17}-C_{21}). Cg4 (C_{22}-C_{27}). Cg5 (N_8 and C_{28}-C_{32}). Cg6 (C_{33}-C_{38}).

Cg⊥ - The perpendicular displacement between two ring centroids measured from Cg1 to the plane parallel with the second ring centroid.

Beta – The ring normal and the vector between the ring centroids.

Table S10. Selected offset π-interaction lengths and angles in **3.**

Interaction	Distance (Å)	Perpendicular Displacement	Distance (Å)	Angle Beta (°)	
$Cg_1 \cdots Cg_{1'}$	3.8079(13)	$Cg_1 \cdots Cg_{1'} \perp$	3.8056(9)	1.6	
$Cg_1 \cdots Cg_3$	3.8218(14)	$Cg_1 \cdots Cg_3 \perp$	3.4492(9)	15.8	
$Cg_2 \cdots Cg_{2'}$	3.8105(13)	$Cg_2 \cdots Cg_{2'} \perp$	3.6158(9)	18.4	
$Cg_2 \cdots Cg_3$	3.8681(14)	$Cg_2 \cdots Cg_3 \perp$	3.6246(9)	25.7	

Cg1 (N_6 and C_6-C_{10}). Cg2 (N_7 and C_{11}-C_{15}). Cg3 (N_8 and C_{16}-C_{20}).

Table S11. Selected interaction distances and angles of **4** and **7**.

Compound 4		
Interaction	**Distance (Å)**	**Angle (°)**
$Ow_2\cdots S_3$	3.292(2)	$C_3{=}S_3\cdots O_{w2}$ 81.35(9)
$N_6\cdots Ow_2$	2.686(3)	
$N_7\cdots Ow_1$	2.835(4)	
$Ow_1\cdots Ow_{1'}$	2.936(7)	
$Ow_{1'}\cdots N_7$	2.835(4)	
$N_6\text{-}H_{6a}\cdots Ow_2$	2.686(3)	
$Ow_2\cdots S_3$	3.292(2)	
Compound 7		
Interaction	**Distance (Å)**	**Angle (°)**
$Ow_2\cdots Cl_1$	3.142(5)	
$N_7\cdots Cl_2$	3.071(5)	$N_7\text{-}H_7\cdots Cl_2$ 159
$N_5\cdots Cl_2$	3.097(5)	$N_5\text{-}H_{5a}\cdots Cl_2$ 141°
$N_6\cdots Ow_1$	2.771(6)	$N_6\text{-}H_{6a}\cdots Ow_1$ 150°
$N_8\cdots Ow_2$	2.660(7)	$N_8\text{-}H_{8a}\cdots Ow_2$ 148°

6. Figures of compounds 3 – 7

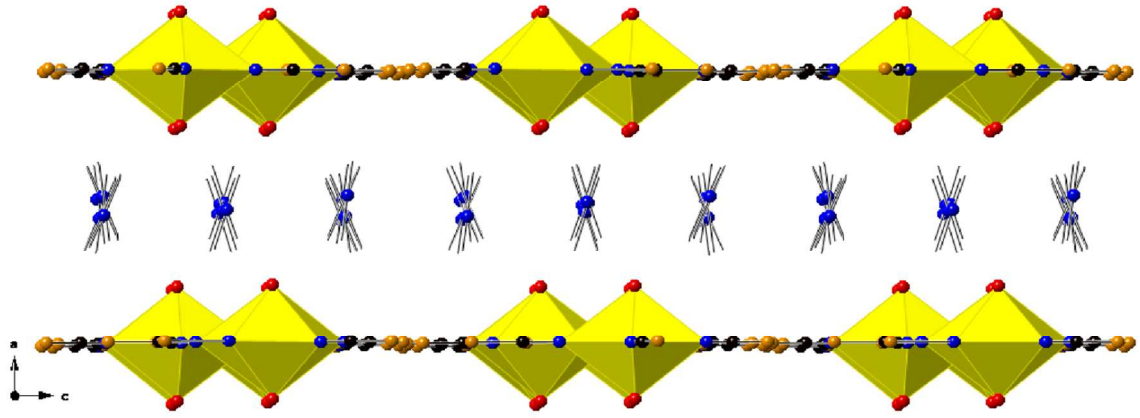

Figure S5. Alternating layers of $[UO_2(NCS)_5]^{3-}$ and 4,4'-BipyH tectons in **3** occupy the (100) plane.

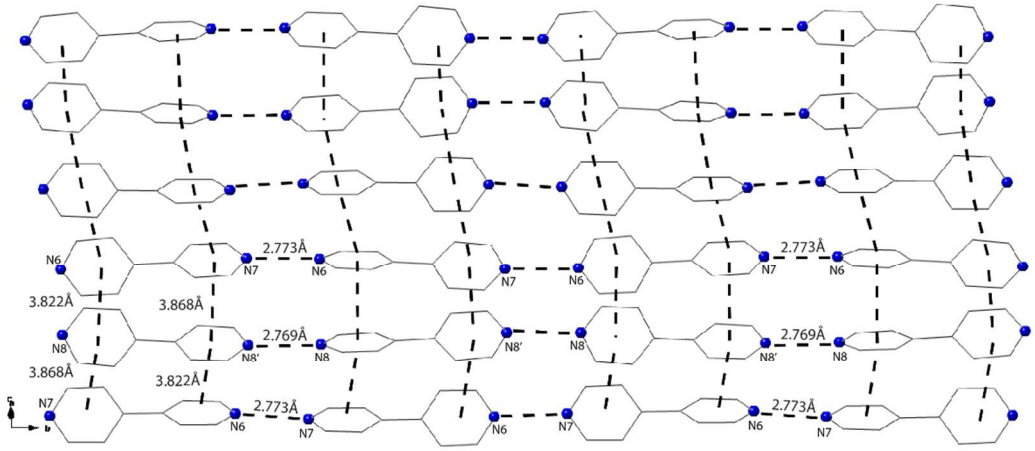

Figure S6. The 4,4'-BipyH cations in **3** form chains via N-H···N hydrogen bonds. The chains run parallel and are linked to one another by offset π-interactions.

*The hydrogen bonding network of **4**, $(C_{10}H_{10}N_2)_{1.5}[UO_2(NCS)_5]$ $2H_2O$:*

A $[UO_2(NCS)_5]^{3-}$ anion is linked to a 4,4'-BipyH_2 cation via a non-coordinated (lattice) water molecule (Ow2) that forms two bridging O-H···S and N-H···O hydrogen bonds (**Figure S7** and **Table S8**). The 4,4'-BipyH_2 cation in turn forms a second N-H···O hydrogen bond to a second water (Ow1) molecule that also forms a second O-H···O hydrogen bond with its symmetry equivalent, Ow_1'. The symmetry equivalent (Ow1') in turn forms a N-H···O hydrogen bond to a second 4,4'-BipyH_2 cation that is then bridged by way of another water molecule (Ow2') to a $[UO_2(NCS)_5]^{3-}$ anion of an adjacent chain.

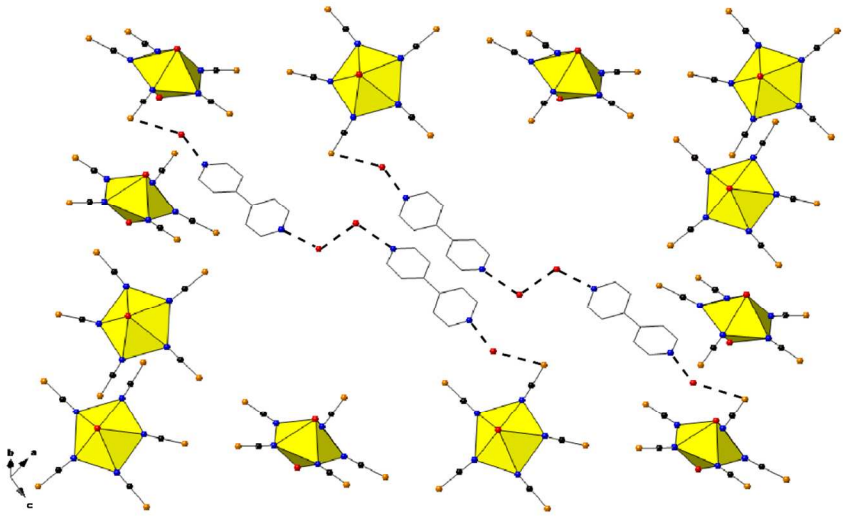

Figure S7. A complex hydrogen bonding network links the $[UO_2(NCS)_5]^{3-}$ tectons of neighboring 'double-wide' chains together. The remaining $[UO_2(NCS)_5]^{3-}$ tectons that comprise the chains have been omitted to highlight the hydrogen bonding network.

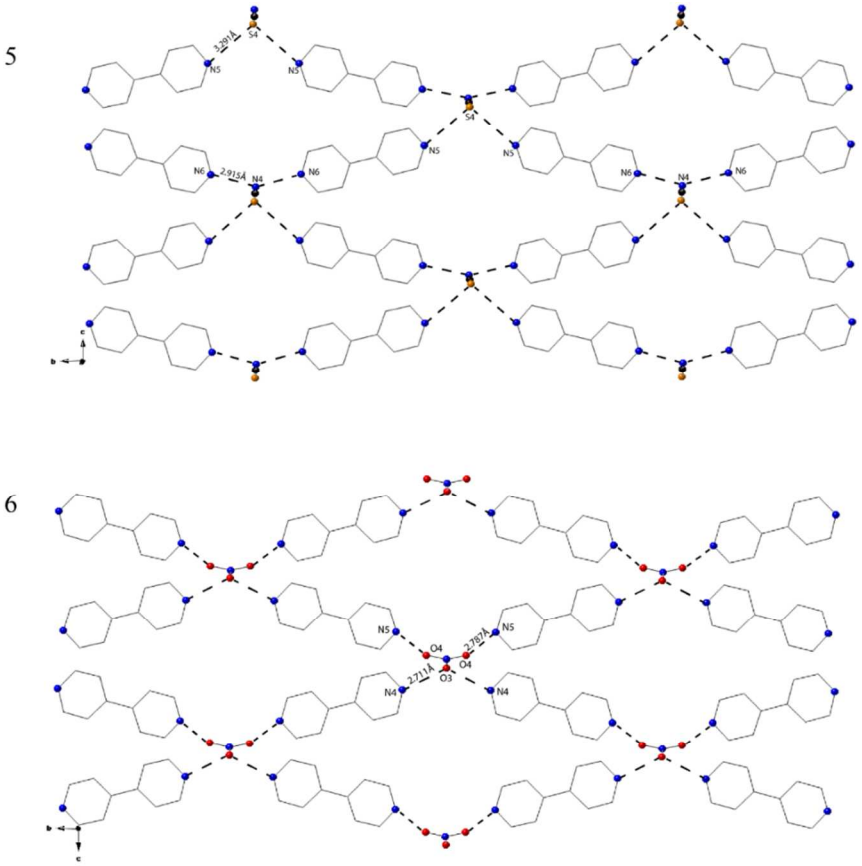

Figure S8. Top: Non-coordinated SCN anions in **5** accept both N-H···N and N-H···S hydrogen bonds from the doubly protonated 4,4-BipyH$_2$ cations to form sheets in the (100) plane. Bottom: The 4,4'-BipyH$_2$ cations in **6** form N-H···O hydrogen bonds with the nitrate anions to form sheets in (100).

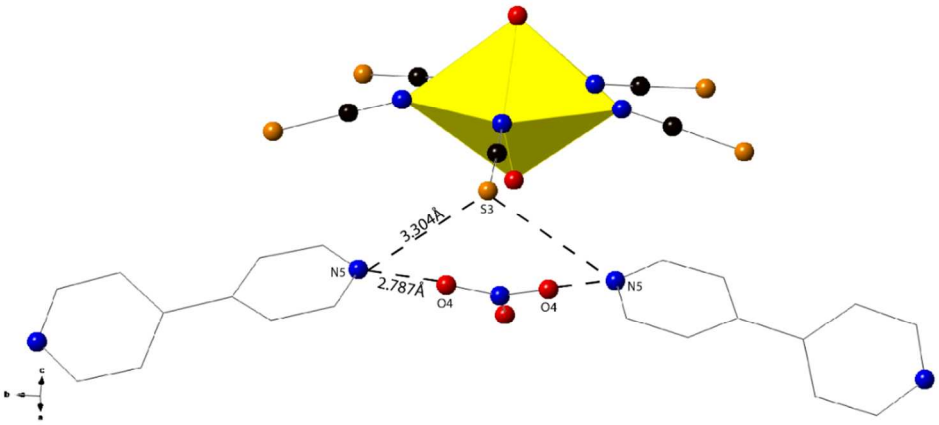

Figure S9. The 4,4'-BipyH_2 cations in **6** form N-H···O and N-H···S hydrogen bonds with the nitrate anions and $[UO_2(NCS)_5]^{3-}$ tectons.

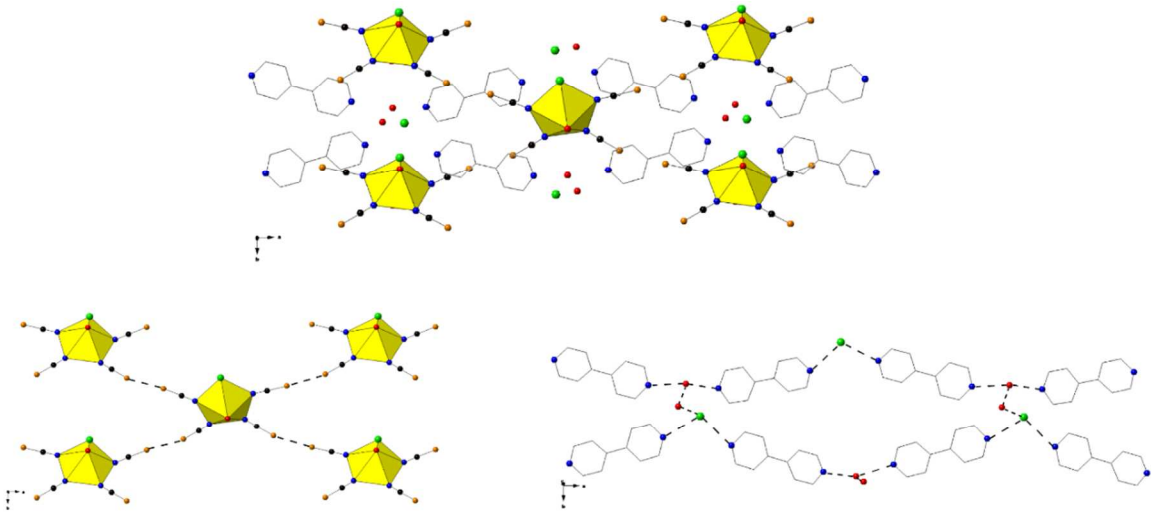

Figure S10. The global structure of **7** (top) with views of the S···S interactions (bottom left) and hydrogen bonding interactions (bottom right) that give rise to the anionic and cation sheet motifs.

7. Electrostatic Potential of the 4-PPH and 4,4'-BipyH/H_2 cations

The electrostatic potential localized on the pyridyl nitrogen atoms of the 4-PPH and 4,4'-BipyH/H_2 cations was quantified to assess hydrogen bond donor strength. The 4-PPH cations crystallize in one of two geometries: linear, where both aromatic rings are coplanar and the twisted, where the phenyl ring is contorted out-of-plane relative to the pyridyl ring (**Figure S11**). The magnitude of the

electrostatic potential of the N-H^+ donor is +581 kJ mol^{-1} in the linear arrangement whereas in the twisted geometry the potential is more positive at +586 kJ mol^{-1} (**Table S12**).

The 4,4'-BipyH/H_2 cations crystallize as a mono or doubly protonated cation. Therefore the 4,4'-BipyH can function as either a hydrogen bond donor and acceptor whereas the 4,4'-BipyH_2 can act as a dual donor (**Figure S11**). The monoprotonated 4,4'-BipyH cation is polar and has a *large* and positive potential at the N-H^+ hydrogen bond donor (+604 kJ mol^{-1}) whereas the non-protonated nitrogen has a smaller potential of +77 kJ mol^{-1} (**Table S12**). The lone pair located on the non-protonated nitrogen offsets some of the positive potential of the cation, allowing for this region to function as a hydrogen bond acceptor as expected. The doubly protonated cation is *not* polar as the magnitude of the ESP at both N-H^+ donors is +851 kJ mol^{-1}. Based solely upon the magnitudes of the electrostatic potentials we rank the hydrogen bond donor strength of the pyridinium cations as follows: 4-PP < 4,4'-BipyH < 4,4'-BipyH_2.

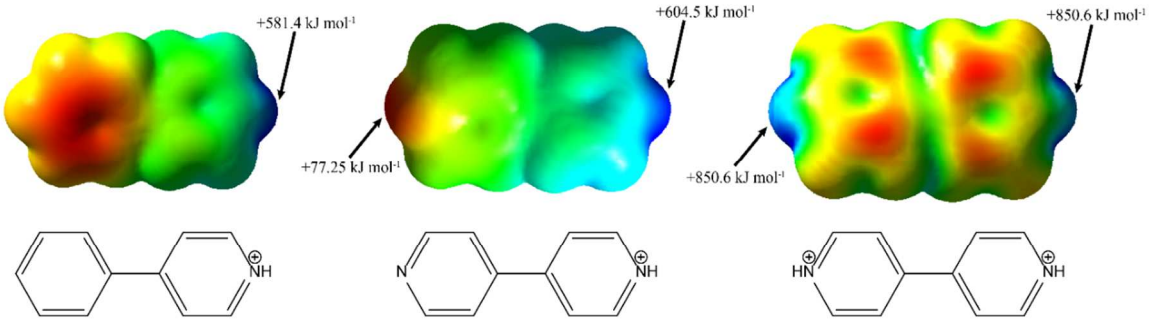

Figure S11. Left-to-Right: The electrostatic potential of the 4-PPH, 4,4'-BipyH and 4,4'-BipyH_2 cations.

Table S12. The ESP at the N-H^+ hydrogen bond donor sites on the pyridinium cations.

Region	4-Phenylpyridine	4,4-Bipyridinium
N-H^+	Linear: +581 kJ mol^{-1} Twisted: +586 kJ mol^{-1}	**Monoprotonated** N1: +604 kJ mol^{-1} N2: +77 kJ mol^{-1} **Doubly Protonated** N1: +851 kJ mol^{-1} N2: +851 kJ mol^{-1}

7. Experimental UV-VIS and Luminescence spectra of 1 – 7

Sample Preparation for Luminescence and Spectroscopy Analysis:

Co-formation of **1-7** is the norm, yet the crystals are easily differentiated by color. Thus, crystals for spectroscopic analysis were manually separated from the bulk product and (if needed) phase purity was assessed via PXRD.

Compound 1: $(C_{11}H_{10}N)_3\,[UO_2(NCS)_5] \cdot 3H_2O$

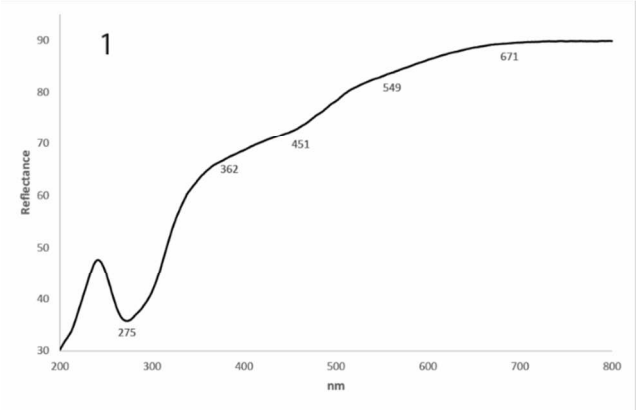

Figure S11. The UV-Vis diffuse reflectance spectrum of **1** features a $SCN \rightarrow UO_2^{2+}$ charge transfer band centered at λ = 490 nm and a maximum at λ = 275 nm that corresponds to the absorbance by the 4-PPH cations.

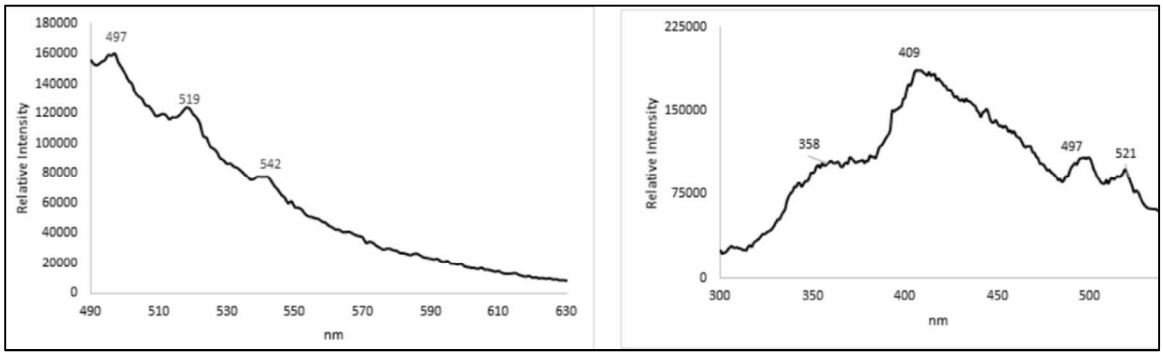

Figure S12. Luminesence spectra of **1** at 77K upon excitation at the UO_2^{2+} λ_{max} of 420 nm (left) and the 4-phenylpyridinium cation λ_{max} of 280 nm (right).

Compound 2: $(C_{11}H_{10}N)_3$ $[UO_2(NCS)_5]$

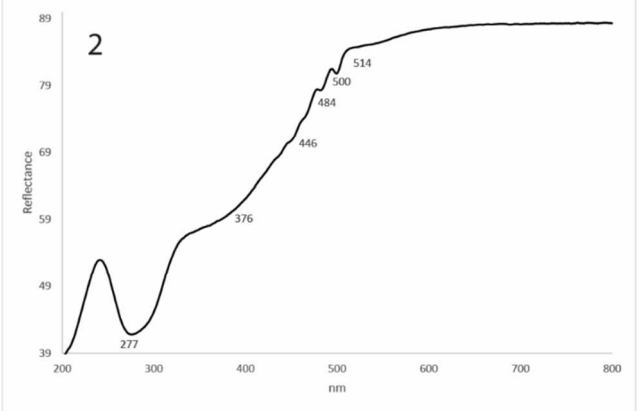

Figure S13. The UV-Vis diffuse reflectance spectrum of **2** features a $SCN \rightarrow UO_2^{2+}$ charge transfer band centered at $\lambda = 440$ nm and maxima at $\lambda = 277$ nm that correspond to the absorbance by 4-PPH.

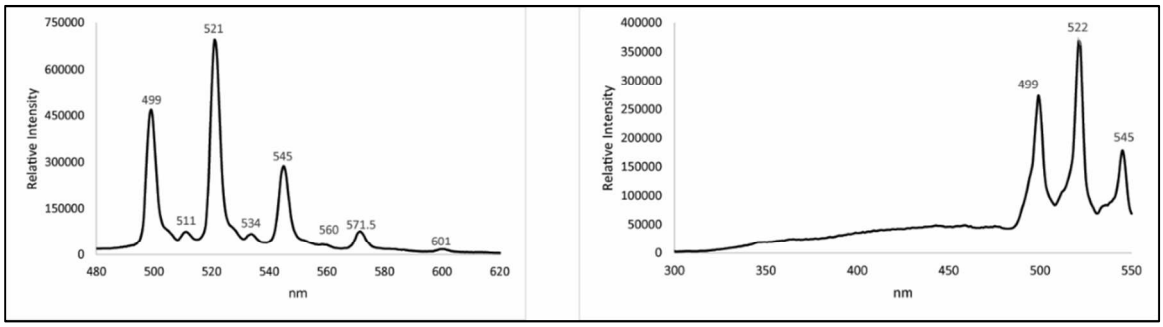

Figure S14. Luminescence spectra of **2** at 77K upon excitation at the UO_2^{2+} λ_{max} of 420 nm (left) and the 4-phenylpyridinium cation λ_{max} of 286 nm (right).

Compound 3: $[C_{10}H_9N_2]_3[UO_2(NCS)_5]$

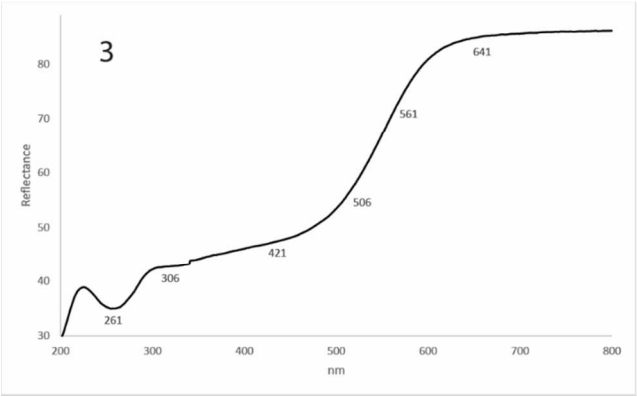

Figure S15. The UV-Vis diffuse reflectance spectrum of **3** features a SCN→UO_2^{2+} charge transfer band centered at λ = 540 nm and maxima at λ = 261 nm that correspond to the absorbance by 4,4'-BIPYH cations.

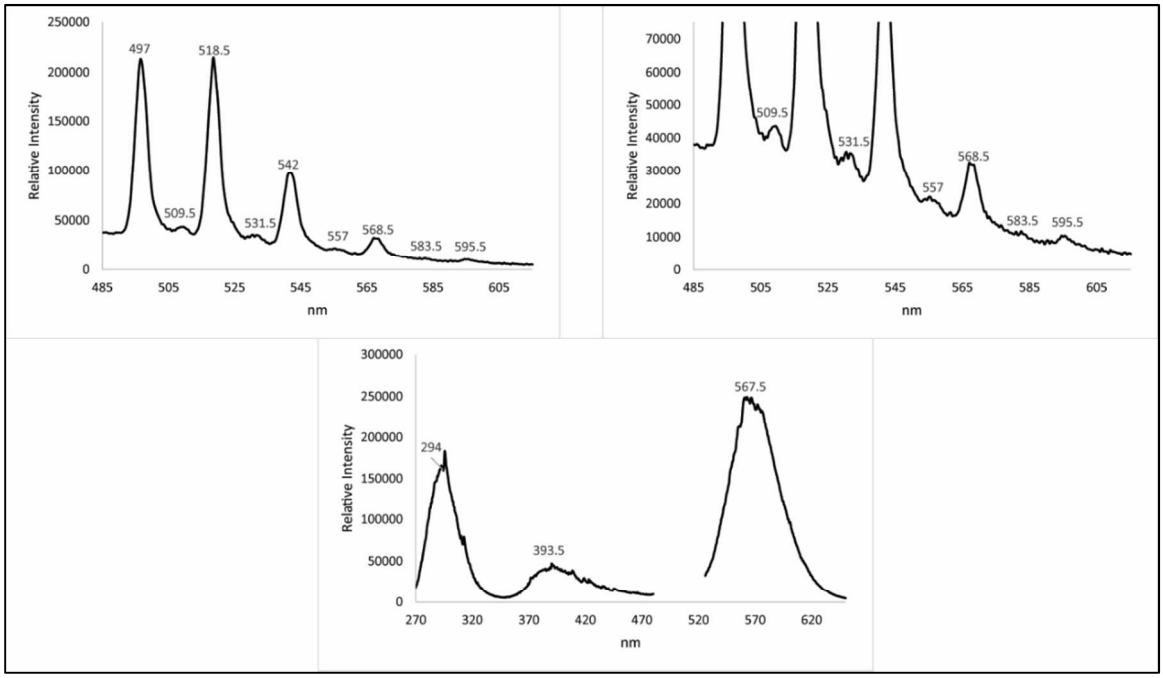

Figure S16. Luminescence spectra of **3** at 77K upon excitation at the UO_2^{2+} λ_{max} of 420 nm (top left); the spectrum is magnified (right) to highlight the vibronic peaks at 509.5, 531.4, 557 and 583.5 nm. Excitation of **3** at the 4,4'-Bipy λ_{max} of 250 nm (bottom) results in 4,4'-Bipyridinium fluoresence and phosphoresence.

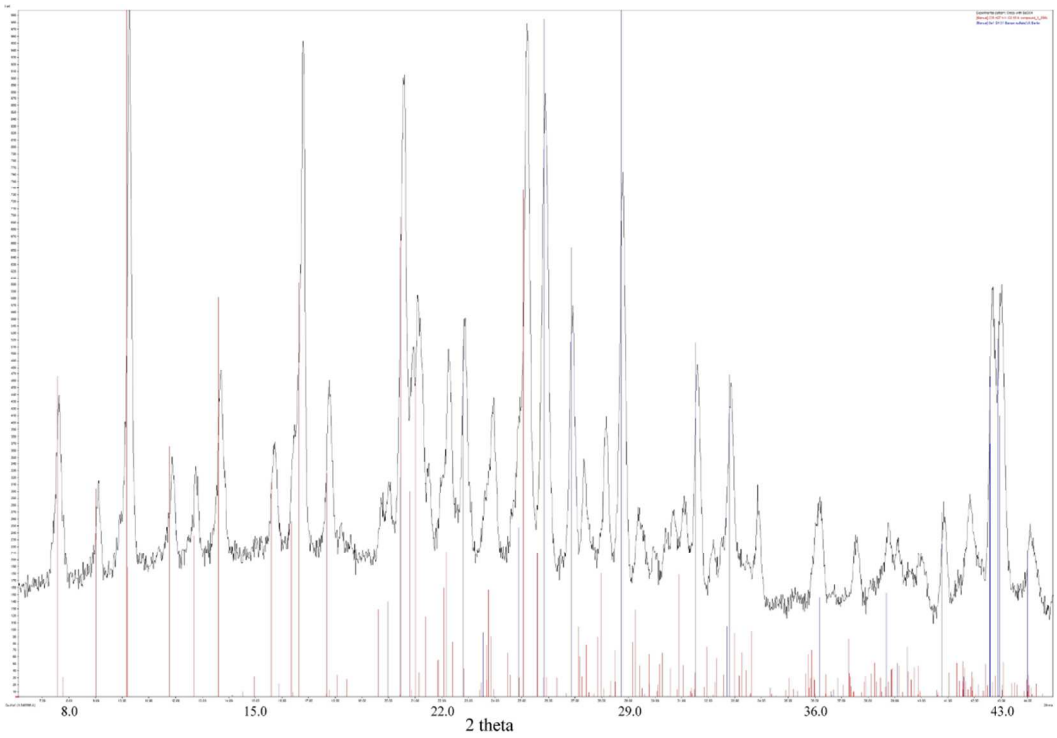

Diffractogram 1. Crystal of **3** were ground in $BaSO_4$ prior to UV-Vis analysis and do not show any signs of a compositional change as a resul of sample preparation. The calculated powder X-ray diffraction pattern based on the single crystal data of **3** and $BaSO_4$ are overlain in red and blue, respectively.

Compound 4: $(C_{10}H_{10}N_2)_{1.5}[UO_2(NCS)_5] \cdot 2H_2O$

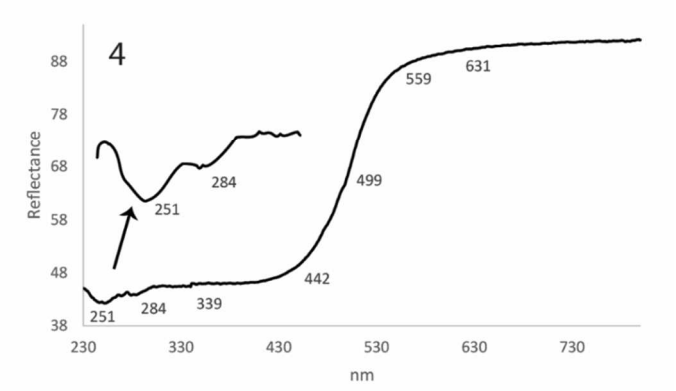

Figure S17. The UV-Vis diffuse reflectance spectrum of **4** features a $SCN \rightarrow UO_2^{2+}$ charge transfer band centered at λ = 490 nm and maxima at λ = 251 nm that correspond to absorption by the 4,4'-BipyH_2 cations.

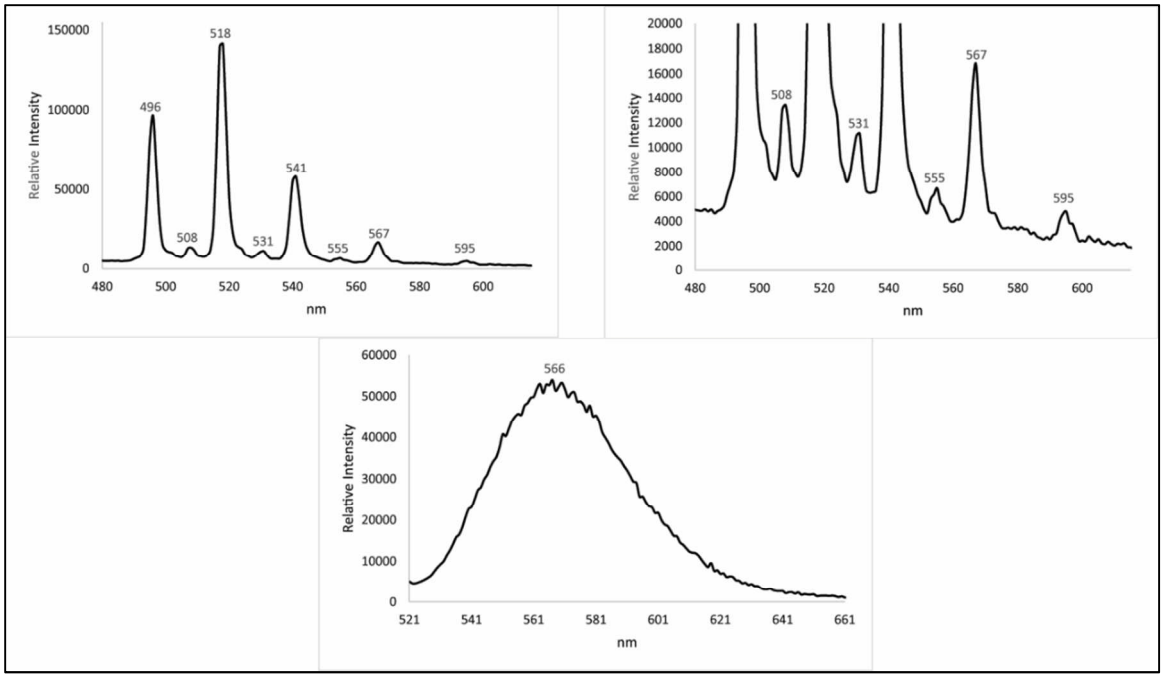

Figure S18. Luminescence spectra of **4** at 77K upon excitation at the UO_2^{2+} λ_{max} of 420 nm (top left); the spectrum is magnified (right) to highlight the vibronic peaks at 508, 531 and 555 nm. Excitation of **4** at the 4,4'-Bipy λ_{max} of 250 nm (bottom) results in 4,4'-Bipyridinium phosphoresence.

Compound 5: $(C_{10}H_{10}N_2)_2[UO_2(NCS)_4(SCN)_{0.75}(Cl)_{0.25}] \cdot (SCN)$

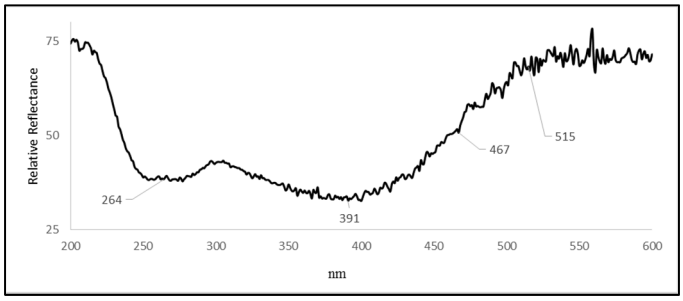

Figure S19. The UV-Vis diffuse reflectance spectrum of **5** features a SCN→UO_2^{2+} charge transfer band centered at λ = 467 nm and maxima at λ = 264 nm that correspond to the absorption by 4,4'-BipyH_2 cations.

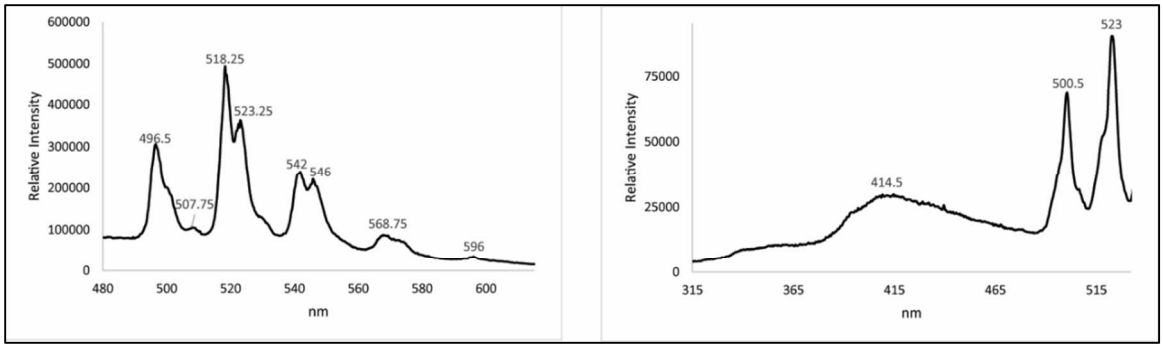

Figure S20. Luminescence spectra of **5** at 77K upon excitation at the UO_2^{2+} λ_{max} of 420 nm (left) and the 4,4'-Dipyridyl λ_{max} of 276 nm (right).

Compound 6: $(C_{10}H_{10}N_2)_2[UO_2(NCS)_5] \cdot NO_3$

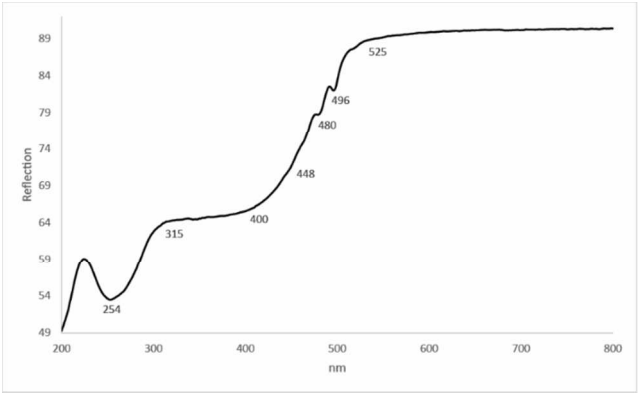

Figure S21. The UV-Vis diffuse reflectance spectrum of **6** features a SCN→UO_2^{2+} charge transfer band centered at λ = 448 nm and λ = 254 nm that correspond to the absorption by the 4,4'-BipyH_2 cations.

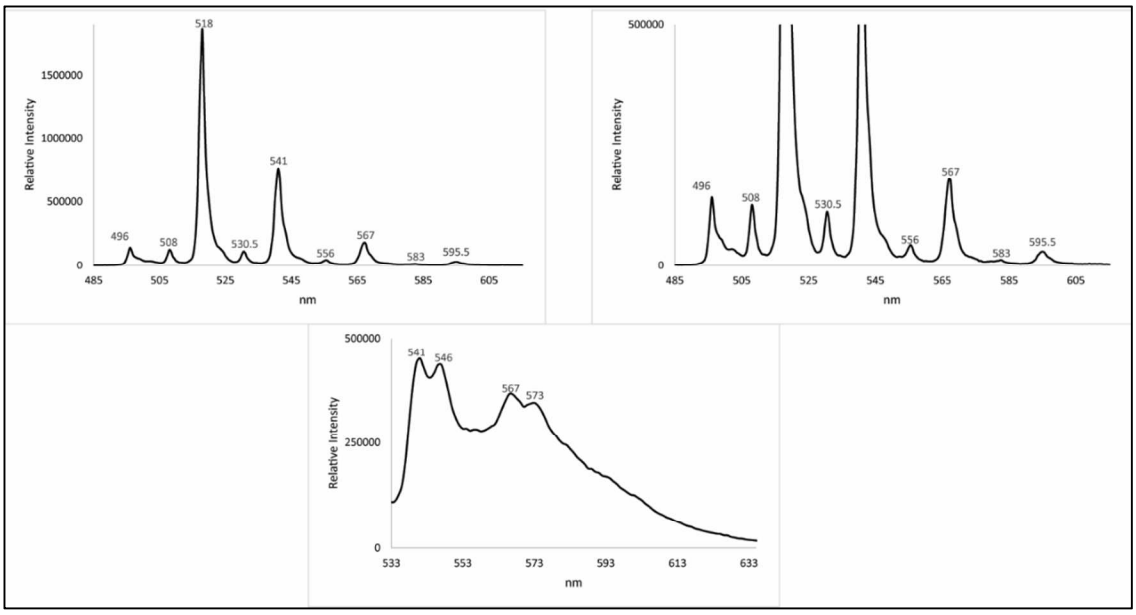

Figure S22. The luminescence spectra of **6** at 77 K upon excitation at the UO_2^{2+} λ_{max} of 420 nm (top left); the spectrum is magnified (right) to highlight the vibronic peaks at 496, 50, 530.5, 556, 583 and 595.5 nm. Excitation of **6** at the 4,4'-Bipy λ_{max} of 250 nm (bottom) results in a UO_2^{2+} and 4,4'-bipyridinium based luminesence.

Compound 7: $(C_{10}H_{10}N_2)_2[UO_2(NCS)_4Cl] \cdot Cl \cdot 2H_2O$

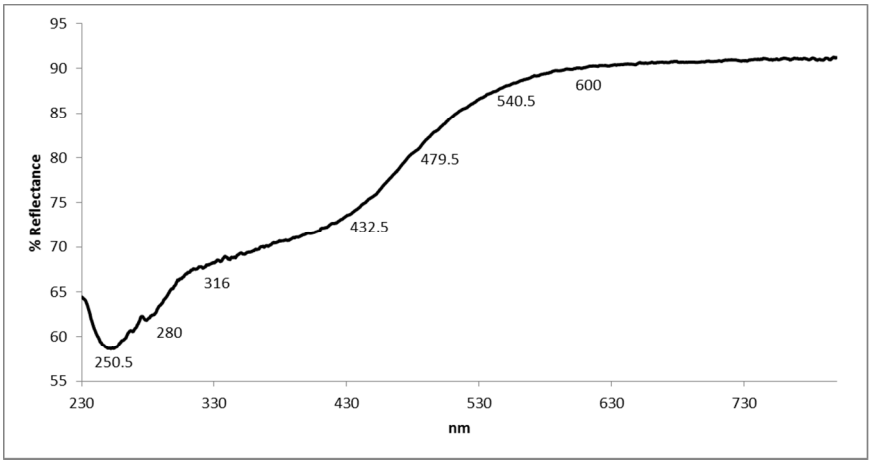

Figure S23. The UV-Vis diffuse reflectance spectrum of **7** features a SCN → UO_2^{2+} charge transfer band centered at λ = 480 nm and maxima at λ = 250 nm that correspond to the absorption by 4,4'-BipyH_2 cations.

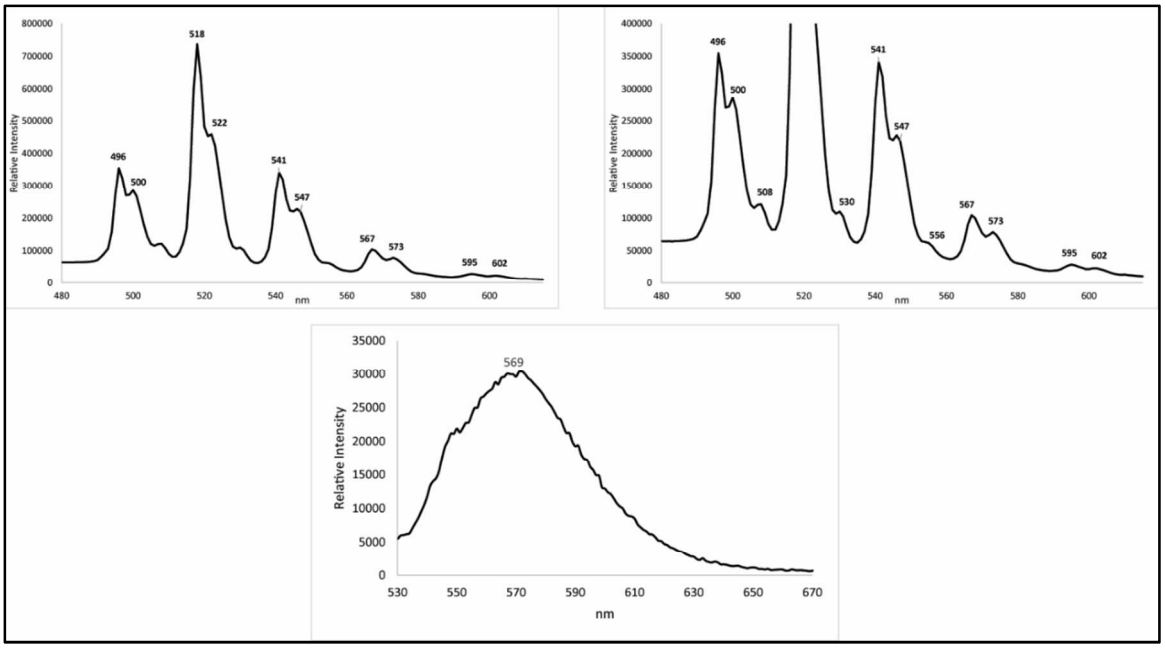

Figure S24. The luminescence spectra of **7** at 77K upon excitation at the UO_2^{2+} λ_{max} of 420 nm (top left); the spectrum is magnified (right) to highlight the shoulders (500, 547, 573 and 603 nm) and the less intense vibronic peaks: 508, 530, 556 and 595 nm. Excitation of **7** at the 4,4'-Bipy λ_{max} of 254 nm (bottom) results in 4,4'-bipyridinium luminesence.

9. Low Temperature and calculated UV-Vis spectra of 3 and other related information

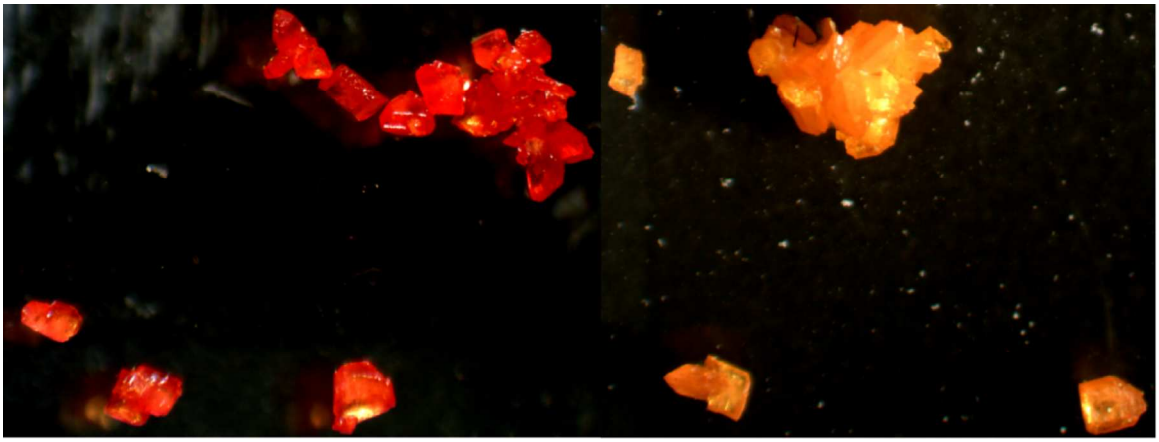

Photo S3. The crystals of **3** are red to 298K (left) and light orange (right) at 77K.

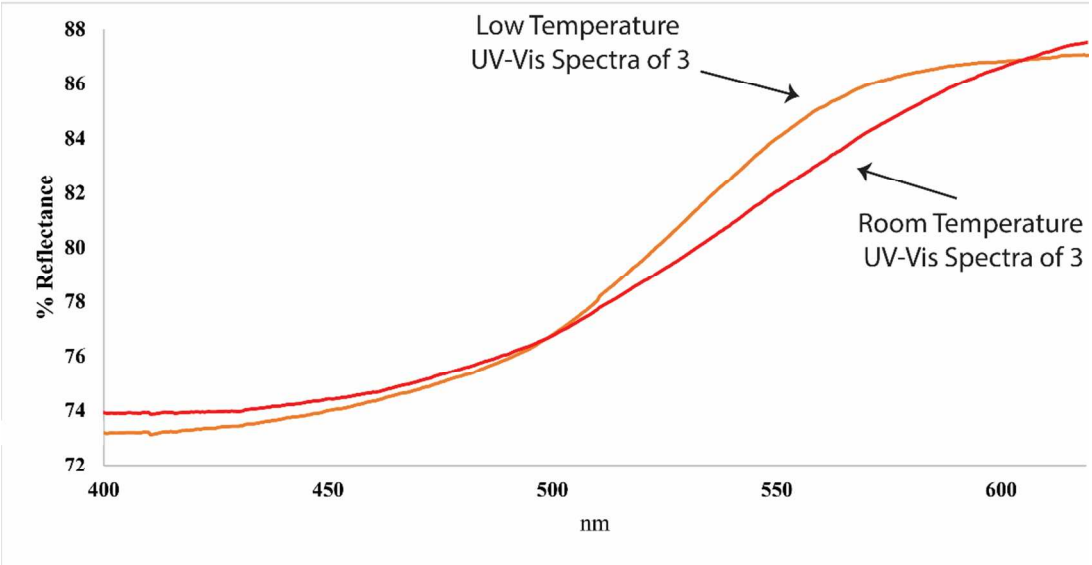

Figure S25. The experimental diffuse reflectance spectra of **3** at 298K (red trace) and low-temperature (orange trace).

After the room temperature UV-Vis diffuse reflectance data were collected the specimen (including the sample holder) was immersed in liquid nitrogen for approximately three minutes. The sample holder was quickly removed from the liquid nitrogen and placed into the instrument and data collected. The temperature of the sample holder was recorded at the beginning (-44°C) and end (-19°C) of the data collection using a laser infrared thermometer. We note that whereas this experiment is qualitative, the low-temperature spectrum was taken in triplicate, i.e. the sample holder was cooled each time, and the data were nearly identical. Moreover, the experiment was reproducible as the sample was allowed to warm to room temperature between each measurement

cycle.

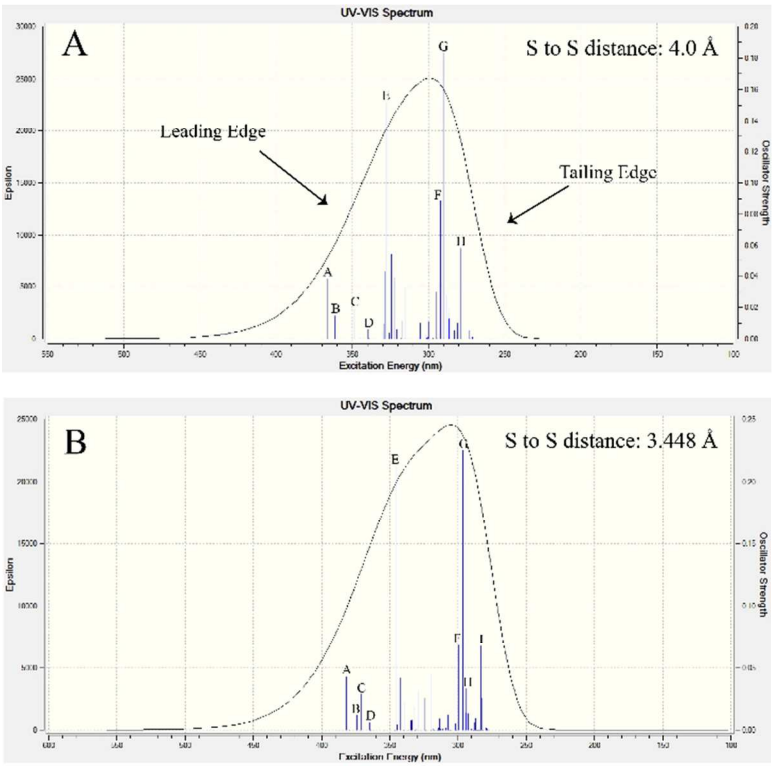

Figure S26. The calculated UV-Vis absorbance spectra of **A** and **B**

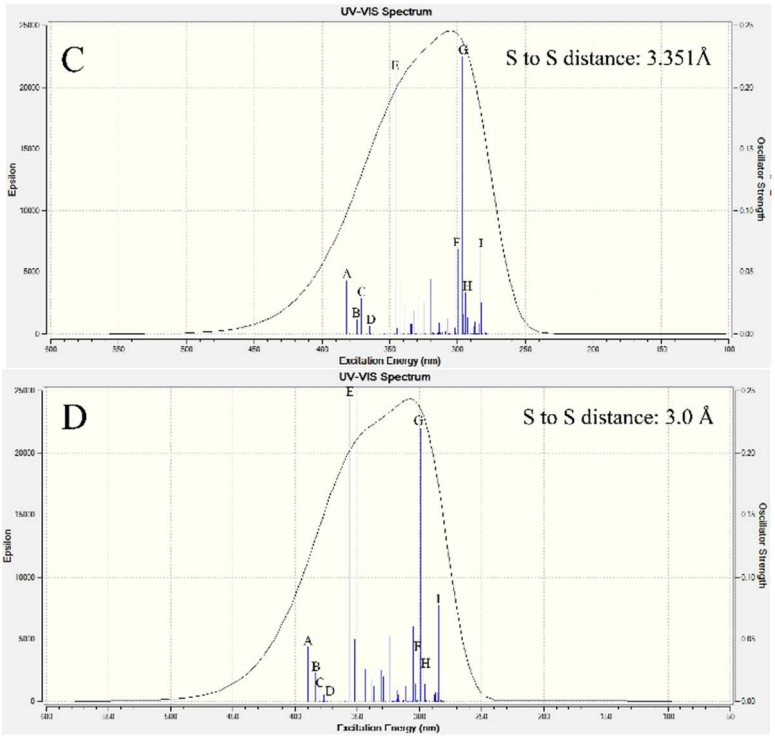

Figure S27. The calculated UV-Vis absorbance spectra of **C** and **D**.

Table S13. The major electronic and molecular orbital transitions from calculated Spectrum A.

Spectrum A: S···S 4.000 Å Distance	**Energy of the transition and its relative Contribution**	**Position and Nature of the Transition**	**Oscillator Strength**
A: Excited State 1	3.3835 eV	366.43 nm	f = 0.0382
285 → 300	0.11004	Intra	
290 → 295 LUMO	**0.64326**	**Intra**	
290 → 303	0.12953	Intra	
292 → 295 LUMO	0.17661	Inter	
B: Excited State 4	3.4322 eV	361.23 nm	f = 0.0146
290 → 303	**0.64855**	**Intra**	
292 → 303	0.16437	Intra	
C: Excited State 7	3.5560 eV	348.66 nm	f = 0.0184
255 → 302	0.13533	Intra	
288 → 301	**0.42963**	**Intra**	
D: Excited State 12	3.65120 eV	339.57 nm	f = 0.0060
288 → 296	**0.56989**	**Intra**	
288 → 301	0.26380	Intra	
E: Excited State 21	3.7825 eV	327.78 nm	f = 0.1515
287 → 301	**0.34217**	**Intra**	
288 → 301	0.31646	Intra	
294 HOMO → 296	0.26674	Inter	
294 HOMO → 315	0.28494	Intra	
F: Excited State 65	4.2434 eV	292.18 nm	f = 0.0882
292 → 305	**0.48600**	**Intra**	
292 → 315	0.21788	Intra	
293 → 312	0.30435	Intra	
G: Excited State 66	4.2740 eV	290.09 nm	f = 0.1833
253 → 297	0.11765	Intra	
283 → 303	**0.56069**	**Intra**	
285 → 300	0.16430	Intra	
292 → 315	0.24630	Intra	
H: Excited State 68	4.2968 eV	288.5 nm	f = 0.0268
292 → 315	**0.49102**	**Intra**	
I: Excited State 88	4.4405 eV	279.21 nm	f = 0.0455
264 → 310	0.10668	Intra	
264 → 312	0.13344	Intra	
291 → 310	0.18404	Intra	

291 → 312	0.26002	Intra	
292 → 298	**0.48287**	**Intra**	
292 → 315	0.14554	Intra	
294 HOMO → 298	0.13929	Intra	
I': Excited State 89	4.4416 eV	279.14 nm	f = 0.0582
260 → 312	0.10668	Intra	
289 → 312	0.13812	Intra	
292 → 298	**0.40450**	**Intra**	
294 HOMO → 298	0.11581	Intra	

***Denotes a minor contribution.**

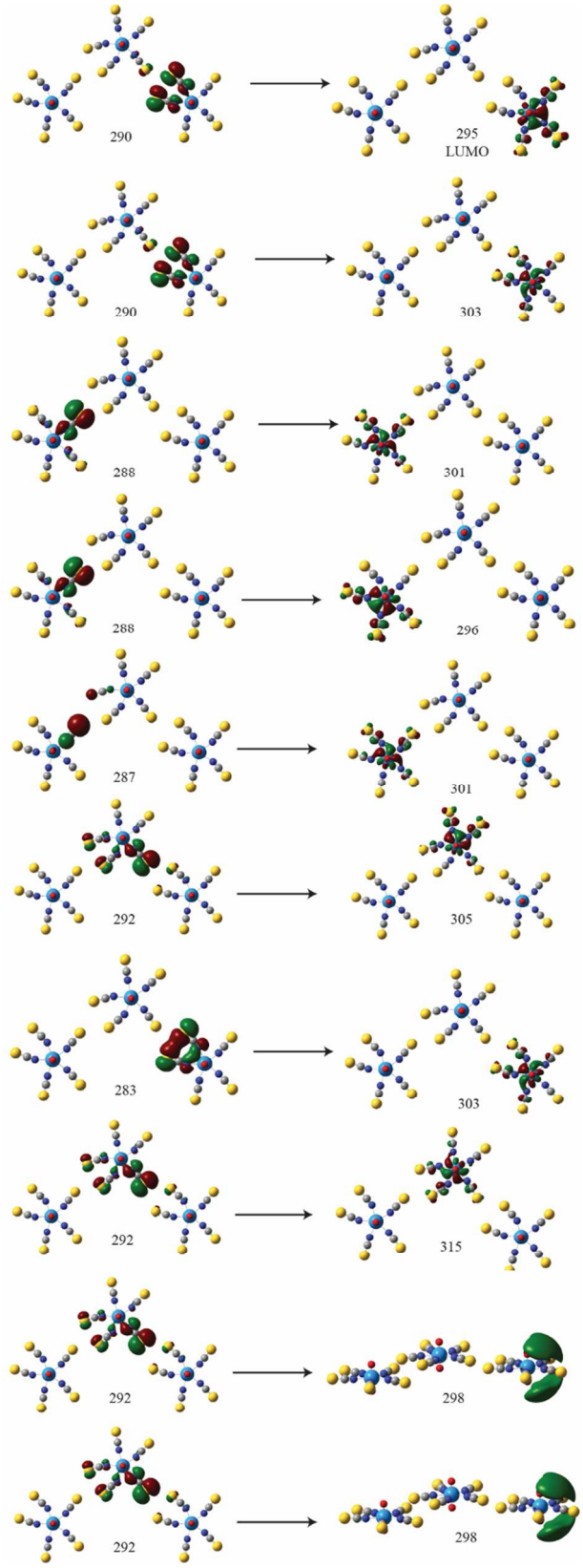

Figure S28. The major molecular orbital transitions that comprise the excited states in the 4.000 Å model.

Table S14. The major electronic and molecular orbital transitions from calculated Spectrum B.

Spectrum B: S···S 3.448 Å Distance	**Energy of the transition and its relative Contribution**	**Position and Nature of the Transition**	**Oscillator Strength**
A: Excited State 1	3.2547 eV	380.94 nm	f = 0.0432
286 → 299	0.11034	Intra	
290 → 295 LUMO	**0.56436**	**Intra/Inter**	
B: Excited State 4	3.3220 eV	373.22 nm	f = 0.0122
290 → 303	**0.58580**	**Intra/Inter**	
C: Excited State 6	3.3613 eV	368.86 nm	f = 0.0285
289 → 301	**0.36641**	**Intra**	
293 → 302	0.140585	Intra	
294 HOMO → 301	0.17718	Intra	
D: Excited State 9	3.4200 eV	362.53 nm	f = 0.0061
288 → 296	**0.47366**	**Intra**	
288 → 301	0.30207	Intra	
294 HOMO → 296	0.30654	Intra	
294 HOMO → 301	0.14100	Intra	
E: Excited State 16	3.6044 eV	343.98 nm	f = 0.2063
287 → 302	0.15633	Intra	
288 → 302	**0.40056**	**Intra**	
289 → 301	0.27940	Inter	
294 HOMO → 301	0.30267	Intra	
F: Excited State 64	4.1437 eV	299.21 nm	f = 0.0661
290 → 306	0.10504	Intra	
291 → 313	0.21499	Intra	
291 → 306	**0.46772**	**Intra**	
G: Excited State 68	4.1830 eV	296.40 nm	f = 0.2007
247 → 302	0.12450	Intra	
257 → 302	0.10508	Intra	
283 → 303	**0.52077**	**Intra**	
292 → 303	0.17912	Intra	
G': Excited State 69	4.1851 eV	296.25 nm	f = 0.0237
269 → 302	0.13211	Intra	
275 → 302	0.12879	Inter	
279 → 302	**0.15447**	**Inter**	
283 → 303	0.15072	Inter	
H: Excited State 73	4.2218 eV	293.67 nm	f = 0.0556

264 → 312	0.11141	Intra	
283 → 303	0.16017	Inter	
290 → 315	0.11370	Intra/Inter	
291 → 313	0.11802	Intra/Inter*	
292 → 303	0.12315	Inter	
292 → 315	**0.47701**	**Intra/Inter**	
I': Excited State 90	4.3856 eV	282.71 nm	f = 0.0858
260 → 312	0.12092	Intra	
264 → 313	0.26218	Intra	
287 → 312	0.10440	Inter	
291 → 313	**0.38266**	**Iner/Intra**	
292 → 315	0.17233	Inter/Intra	

***Denotes a minor contribution.**

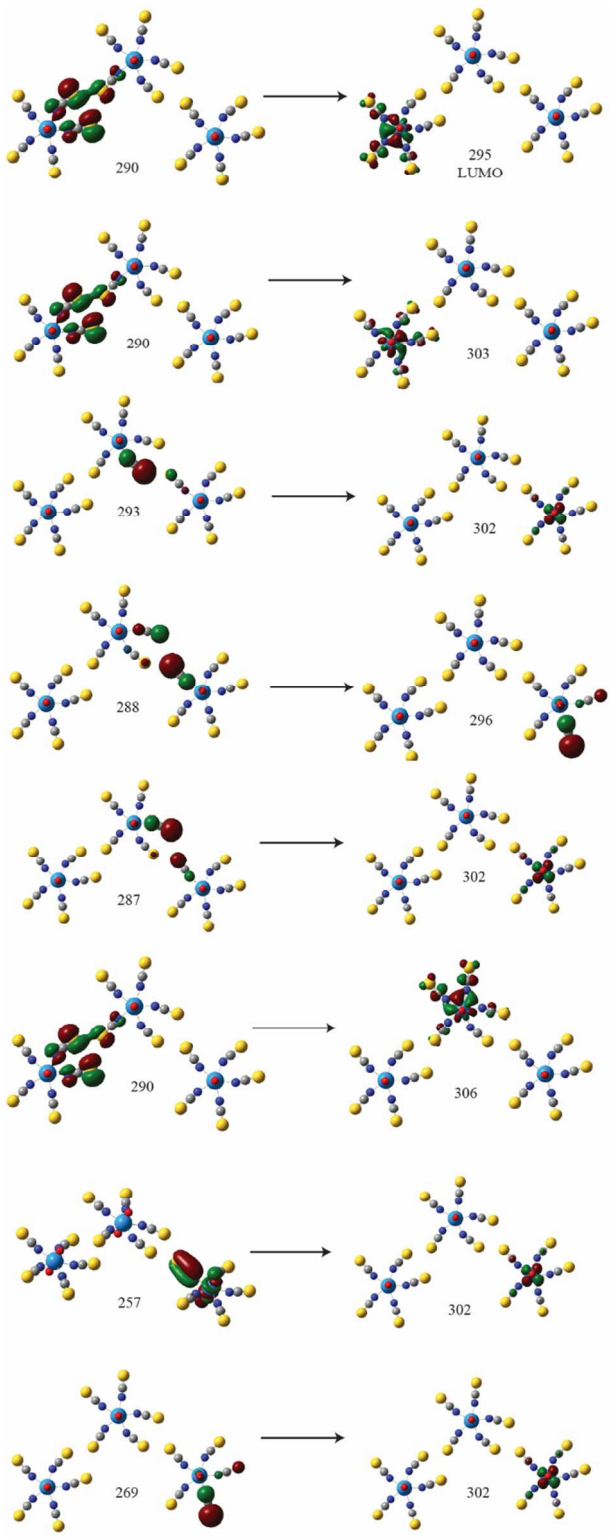

Figure S29. The major molecular orbital transitions that comprise the excited states in the 3.448(3) Å model.

Table S15. The major electronic and molecular orbital transitions from calculated Spectrum C.

Spectrum C: S···S 3.351 Å Distance	**Energy of the transition and its relative Contribution**	**Position and Nature of the Transition**	**Oscillator Strength**
A: Excited State 1	3.2447 eV	382.11 nm	f = 0.0429
290 → 295 LUMO	**0.56424**	**Inter**	
292 → 295 LUMO	0.34043	Inter	
B: Excited State 4	3.3128 eV	374.26 nm	f = 0.0119
290 → 303	**0.58471**	**Inter**	
292 → 303	0.32047	Inter	
C: Excited State 6	3.3613 eV	371.11 nm	f = 0.0285
289 → 301	**0.35496**	**Intra**	
293 → 302	0.16053	Inter	
294 HOMO → 296	0.19606	Inter	
D: Excited State 9	3.3977 eV	364.91 nm	f = 0.0062
288 → 296	**0.46584**	**Inter/Intra**	
288 → 301	0.29856	Intra/Inter	
E: Excited State 16	3.5853 eV	343.98 nm	f = 0.2122
287 → 302	**0.34217**	**Inter**	
288 → 302	0.31646	Inter	
289 → 301	0.26674	Intra	
294 HOMO → 296	0.28494	Inter	
F: Excited State 65	4.1342 eV	299.90 nm	f = 0.0680
291 → 313	0.22103	Intra/Inter	
292 → 306	**0.46881**	**Intra/Inter**	
292 → 314	0.27964	Intra/Inter	
G: Excited State 68	4.1797 eV	296.63 nm	f = 0.2250
283 → 303	**0.54479**	**Intra**	
292 → 314	0.23238	Intra/Inter	
G': Excited State 70	4.1855 eV	296.22 nm	f = 0.0160
269 → 302	0.13699	Inter/ yl*	
276 → 302	0.13307	Inter/ yl*	
279 → 302	**0.16060**	**Inter/ yl***	
H: Excited State 74	4.3856 eV	283.07 nm	f = 0.0858
283 → 303	0.11141	Intra	
293 → 299	**0.16017**	**Inter**	
H': Excited State 90	4.3799 eV	283.07 nm	f = 0.0678

260 → 311	0.11383	Intra	
264 → 313	0.25442	Intra	
291 → 313	**0.35862**	**Iner/Inter***	
294 → 310	0.2172	Intra	

***Denotes a minor contribution.**

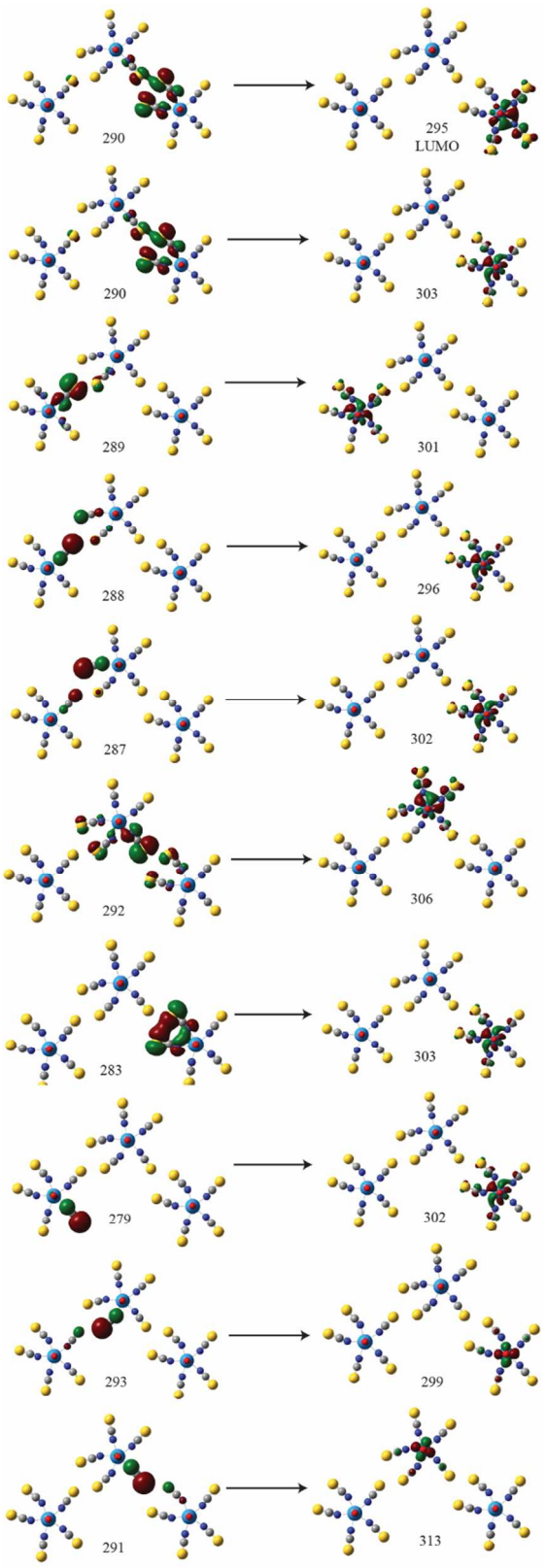

Figure S30. The major molecular orbital transitions that comprise the excited states in the 3.351(1) Å model.

Table S16. The major electronic and molecular orbital transitions from calculated Spectrum D.

Spectrum D: S···S 3.000 Å Distance	Energy of the transition and its relative Contribution	Position and Nature of the Transition	Oscillator Strength
A: Excited State 2	3.1786 eV	390.06 nm	f = 0.0435
287 → 299	0.10836	Intra/Inter*	
289 → 295 LUMO	**0.42305**	**Inter/Intra**	
B: Excited State 4	3.2348 eV	383.28 nm	f = 0.0231
288 → 302	**0.30766**	**Inter/Intra**	
289 → 297	0.17113	Inter/Intra	
290 → 297	0.27179	Inter/Intra	
294 → 297	0.20006	Inter/Intra*	
C: Excited State 6	3.5560 eV	348.66 nm	f = 0.0184
289 → 302	0.13533	Intra	
289 → 301	**0.42963**	**Intra**	
D: Excited State 9	3.2885 eV	377.02 nm	f = 0.0055
289 → 296	0.24625	Inter/Intra	
289 → 301	0.11760	Inter/Intra	
289 → 304	0.10639	Inter/Intra	
290 → 297	**0.39156**	**Inter/Intra**	
290 → 301	0.18584	Inter/Intra	
290 → 304	0.16803	Inter/Intra	
293 → 302	0.12598	Inter/Intra	
294 → 297	0.29973	Inter/Intra*	
294 → 301	0.11289	Inter/Intra*	
294 → 304	0.10001	Inter/Intra*	
E: Excited State 14	3.4809 eV	356.18 nm	f = 0.2439
257 → 302	0.10793	Intra/ yl*	
293 → 302	**0.35593**	**Inter/Intra**	
294 → 297	0.10708	Inter/Intra	
F: Excited State 70	4.1286 eV	292.18 nm	f = 0.0381
283 → 303	0.24104	Inter	
291 → 299	0.15333	Inter/Intra	
292 → 299	0.12060	Inter/Intra	
293 → 299	**0.59587**	**Inter**	
G: Excited State 71	4.1461 eV	290.09 nm	f = 0.1833
283 → 303	**0.36299**	**Inter**	
293 → 313	0.15748	Inter/Intra	
H: Excited State 72	4.1713 eV	288.5 nm	f = 0.0268

283 → 303	0.28284	Inter	
289 → 303	0.11922	Inter/Intra	
289 → 314	0.10164	Inter/Intra	
291 → 313	0.12239	Inter	
292 → 303	0.25626	Intra/Inter	
292 → 314	**0.36078**	**Intra/Inter**	
I: Excited State 91	4.3523 eV	284.87 nm	f = 0.0779
264 → 311	0.16931	Intra/ yl*	
264 → 313	0.31049	Intra/ yl*	
291 → 311	0.19102	Intra/Inter	
291 → 314	**0.36438**	**Inter**	
292 → 314	0.13526	Intra/Inter	

***Denotes a minor contribution.**

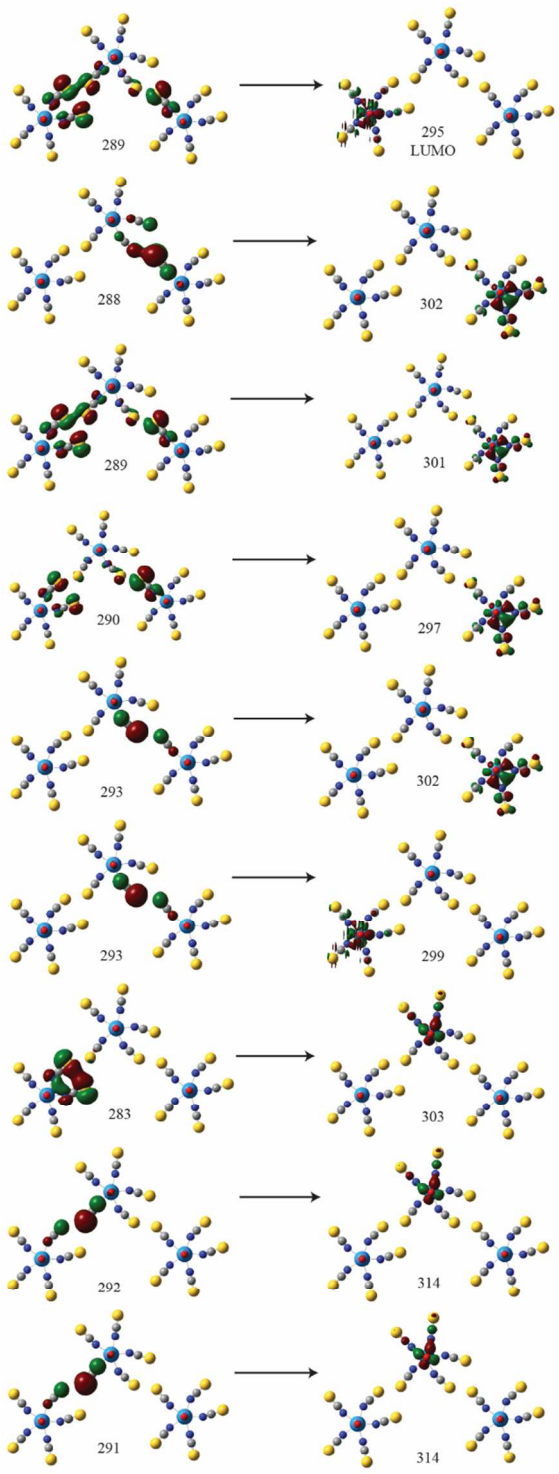

Figure S31. The major molecular orbital transitions that comprise the excited states in the 3.000 Å model.

Table S17. The HOMO – LUMO orbital energy of the system used to calculate spectra **A** – **D**.

Molecular Orbital	3.0 Å S···S Distance	3.351 Å S···S Distance	3.448 Å S···S Distance	4.0 Å S···S Distance
LOMO – 295	13.13 eV	13.0 eV	12.97 eV	12.72 eV
HOMO – 294	8.84 eV	8.67 eV	8.63 eV	8.25 eV
Energy Difference	4.29	4.33	4.34	4.47

10. Calculated Raman and IR Spectroscopy

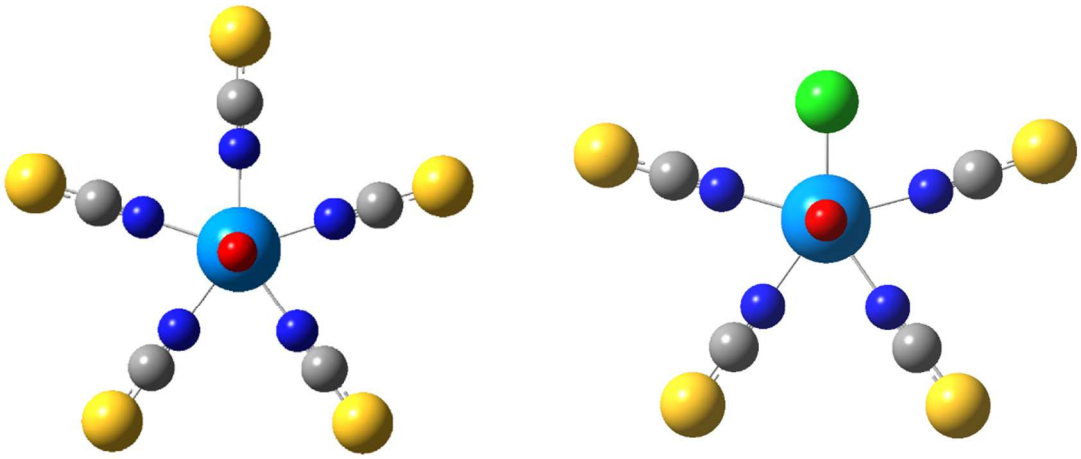

Figure S32. The local coordination geometry of a $[UO_2(NCS)_5]^{3-}$ tecton (from **3**) was optimized prior to the harmonic frequency calculations.

Table S18. Calculated Raman and IR vibrational modes of the $[UO_2(NCS)_5]^{3-}$ and $[UO_2(NCS)_4Cl]^{3-}$ tecton.

	Infrared Frequency	**Mode**	**Raman Frequency**	**Mode**
$[UO_2(NCS)_5]^{3-}$	2230	CN Stretch	2254, 2224, 2212	CN Stretch
	1006	UO Asymmetric Stretch		
	802	CS Stretch	940	UO Symmetric Stretch
	508 - 495	NCS Bending	814	CS Stretch
	286	UO Bending	202	U-NCS Scissoring
	172	U-NCS Stretching	142	U-NCS Stretching
$[UO_2(NCS)_4Cl]^{3-}$				
	2241, 2235	CN Stretch	2258, 2231	CN Stretch
	1005	UO Asymmetric Stretch	939	UO Symmetric Stretch
	791	CS Stretch	803, 793	CS Stretch
	507-497	NCS Bending	Observed in 507-497 range, but very weak	U-NCS Bending
	283, 289	UO Bending	207	U-Cl Stretching With U-NCS Scissoring
	207	U-Cl Stretching With U-NCS Scissoring	194	U-Cl rocking With U-NCS Scissoring
	194	U-Cl rocking With U-NCS Scissoring	138	U-NCS and Cl Stretching
	166, 160	U-NCS Stretching		
	155	U-NCS U-Cl Wagging		
	151	U-NCS Scissoring		

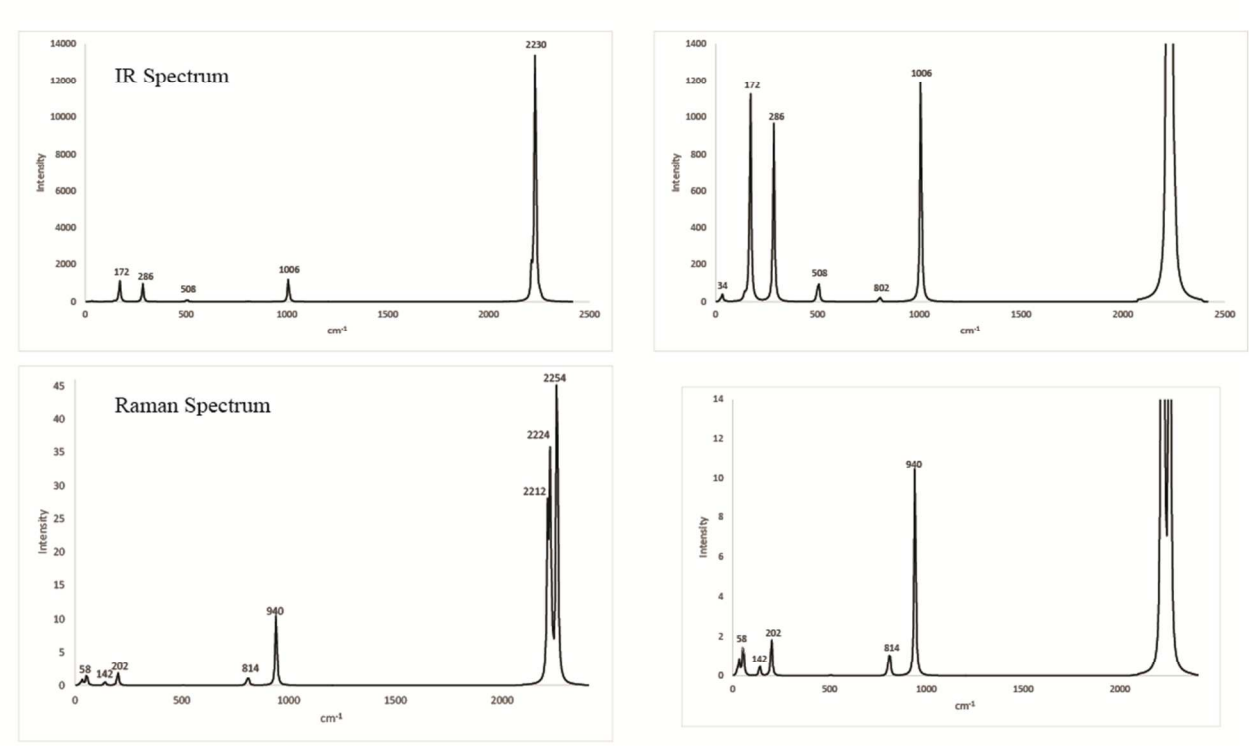

Figure S33. The calculated IR (top) and RAMAN (bottom) spectrum of the optimized $[UO_2(NCS)_5]^{3-}$ tecton. Expanded views of each respective spectrum are on the right.

11. Experimental Raman and IR Spectroscopy

Table S19. Selected experimental Raman and IR vibrational modes of **1 – 7**.

Compound	R νCN (cm^{-1})	R νCS (cm^{-1})	IR νCN (cm^{-1})	IR νCS (cm^{-1})	R ν_1 (UO) (cm^{-1})	ν_3 (UO) (cm^{-1})
1: $(C_{10}H_{10}N)_3[UO_2(NCS)_5] \cdot 3H_2O$	2083, 2056, 2049	802	2060, 2044	811	849	906
2: $(C_{10}H_{10}N)_3[UO_2(NCS)_5]$	2083, 2057, 2049	802	2058, 2044	812	849.5	908
3: $(C_{10}H_9N_2)_3[UO_2(NCS)_5]$	2080, 2052, 2036	808.5	2035	-	836 940	897
4: $(C_{10}H_{10}N_2)_{1.5}[UO_2(NCS)_5] \cdot 2\ H_2O$	2090, 2058, 2027	804.5, 813	2050, 2026	779	837.5	908
5: $(C_{10}H_{10}N_2)_2[UO_2(NCS)_4(NCS)_{0.75}(Cl)_{0.25}]$ □ (SCN)	2094, 2064, 2050	804, 815	2050	773	842	901
7: $(C_{10}H_{10}N_2)_2[UO_2(NCS)_4Cl] \cdot Cl \cdot 2\ H_2O$	2088, 2050	806	2048	779	842	908
6: $(C_{10}H_{10}N_2)_2[UO_2(NCS)_5] \cdot NO_3$	2094, 2084, 2059	810	2048	793	844	901, 914

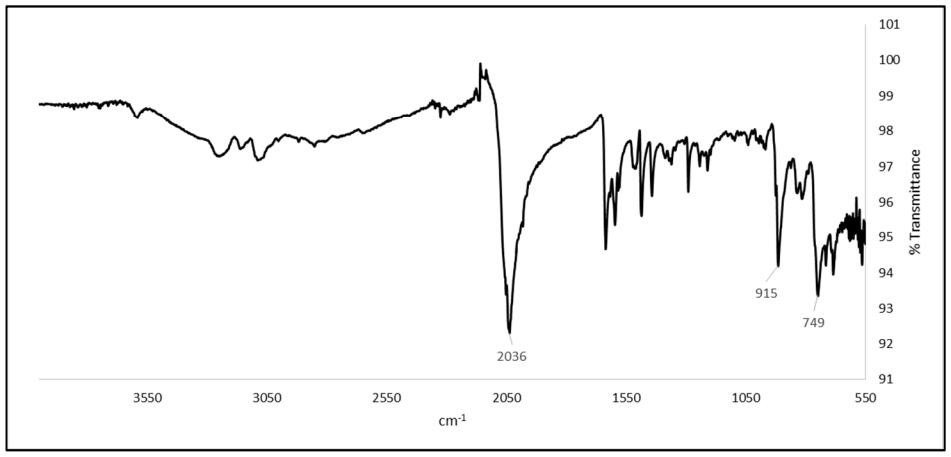

Figure S34. The ATR spectrum of **1**. The ν_1 CN (2036 cm^{-1}), ν_2 CS (749 cm^{-1}) and σ_1 UO_{asym}(915 cm^{-1}) stretching frequencies are labeled.

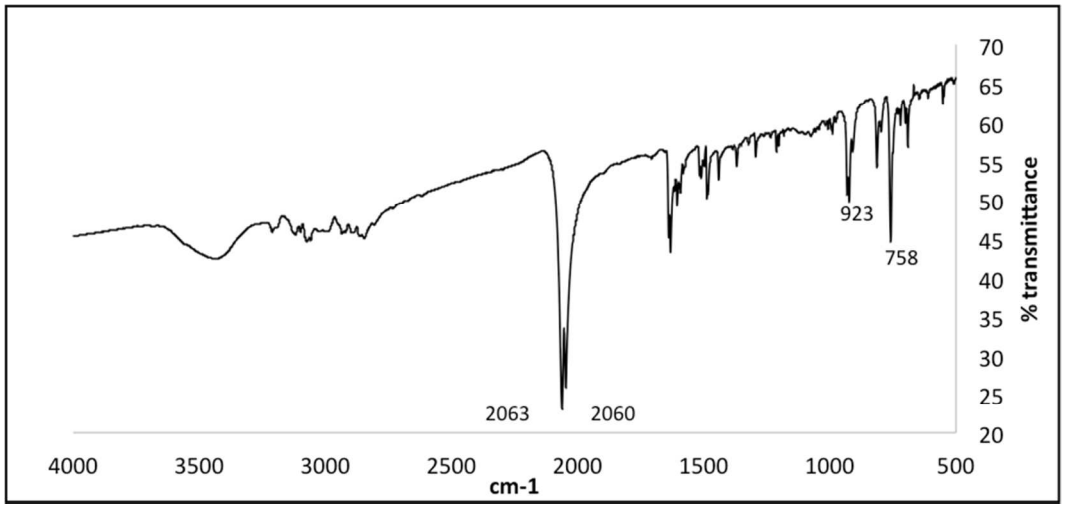

Figure S35. The ATR spectrum of **2**. The ν_1 CN (2063 and 2060 cm^{-1}), ν_2 CS (758 cm^{-1}) and σ_1 UO_{asym}(923 cm^{-1}) stretching frequencies are labeled.

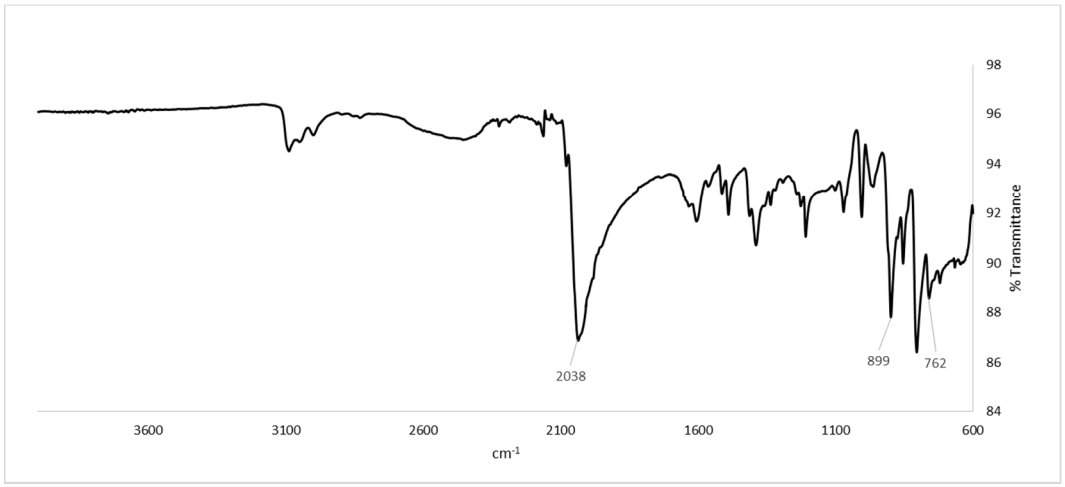

Figure S36. The ATR spectrum of **3**. The ν_1 CN (2038cm^{-1}), ν_2 CS (762cm^{-1}) and σ_1 UO_{asym}(899cm^{-1}) stretching frequencies labeled.

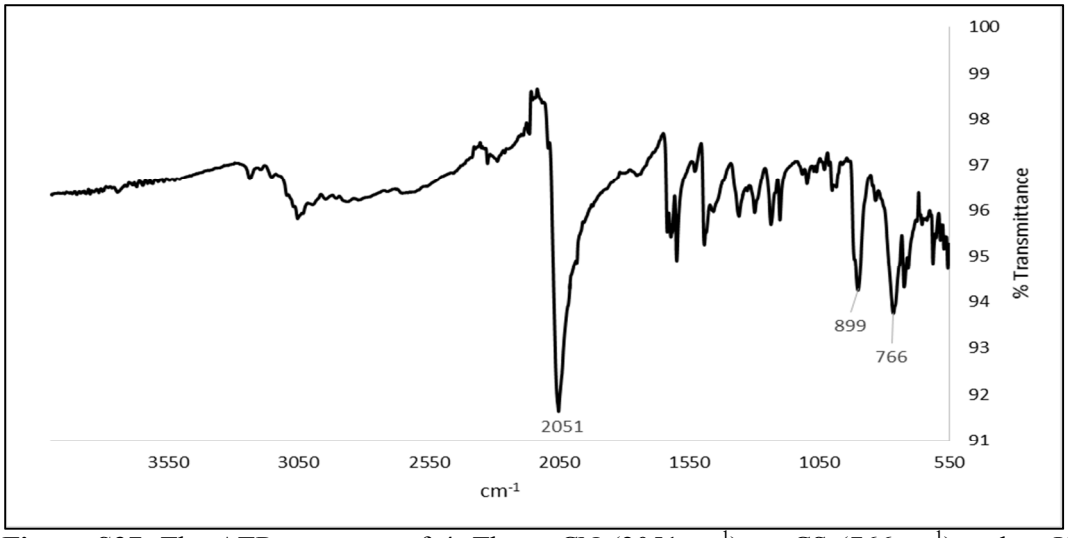

Figure S37. The ATR spectrum of **4**. The ν_1 CN (2051cm^{-1}), ν_2 CS (766cm^{-1}) and σ_1 UO_{asym}(899cm^{-1}) stretching frequencies are labeled.

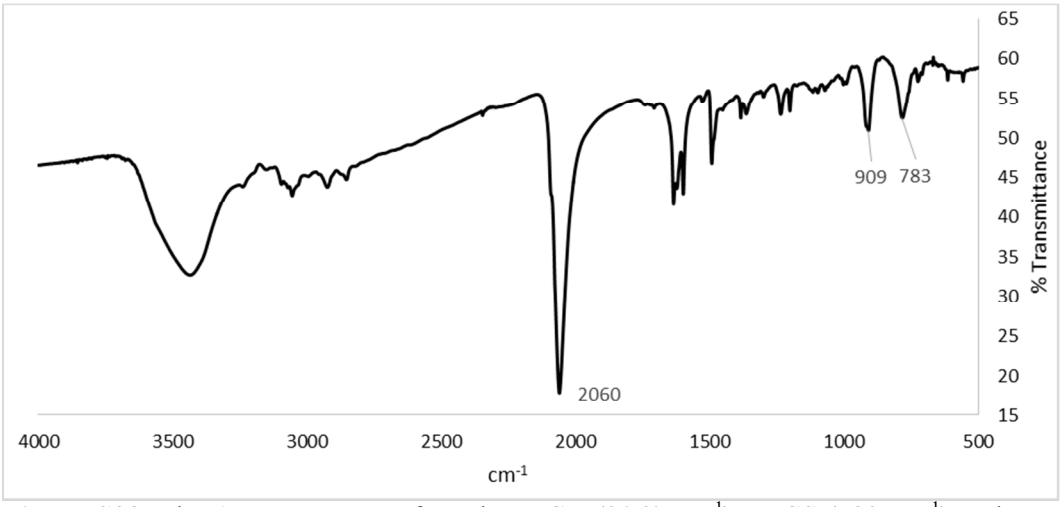

Figure S38. The ATR spectrum of **5**. The ν_1 CN (2060 cm^{-1}), ν_2 CS (783 cm^{-1}) and σ_1 UO_{asym}(909 cm^{-1}) stretching frequencies are labeled.

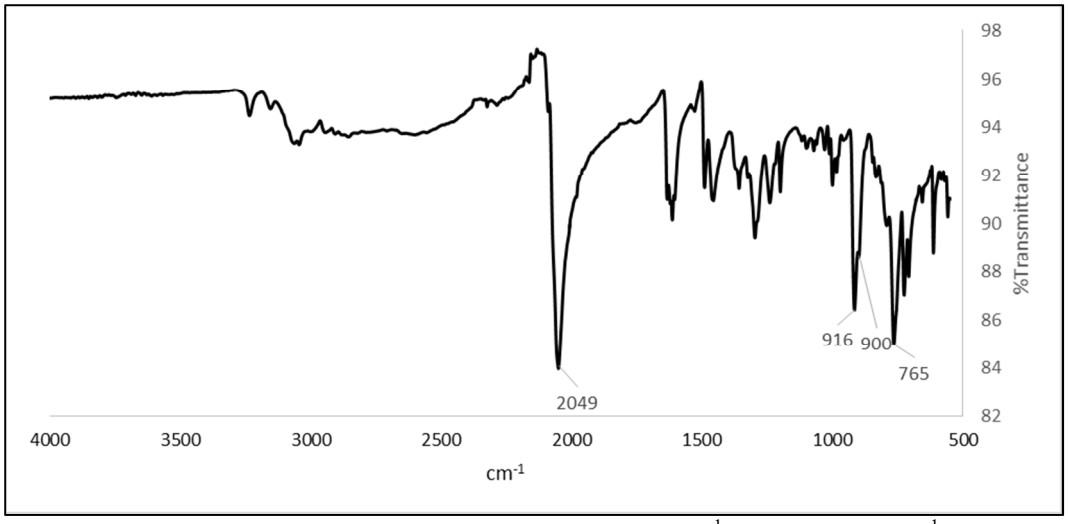

Figure S39. The ATR spectrum of **6**. The ν_1 CN (2049 cm^{-1}), ν_2 CS (765 cm^{-1}) and σ_1 UO_{asym}(916 cm^{-1}) stretching frequencies are labeled.

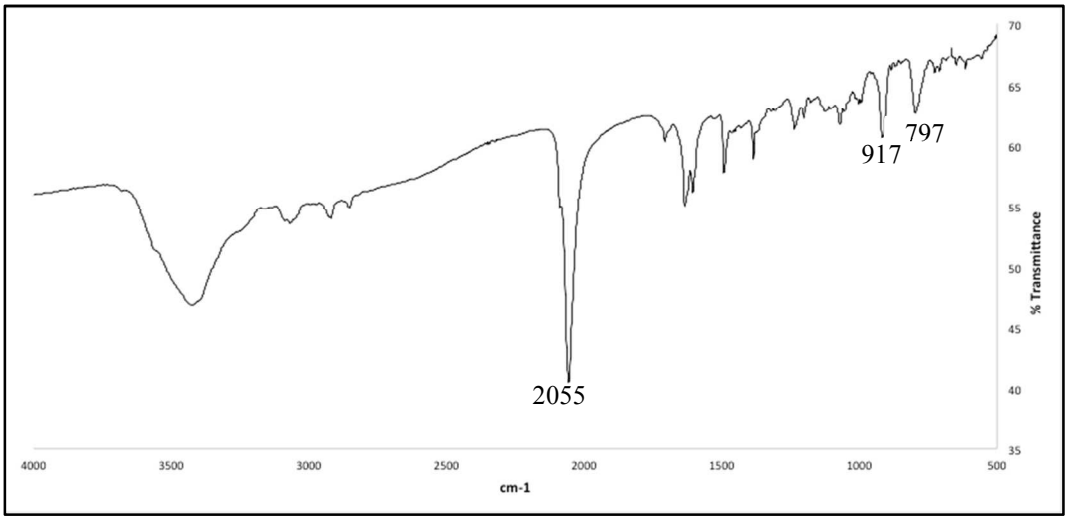

Figure S40. The ATR spectrum of **7**. The ν_1 CN (2055 cm^{-1}), ν_2 CS (797 cm^{-1}) and σ_1 UO_{asym}(917 cm^{-1}) stretching frequencies are labeled.

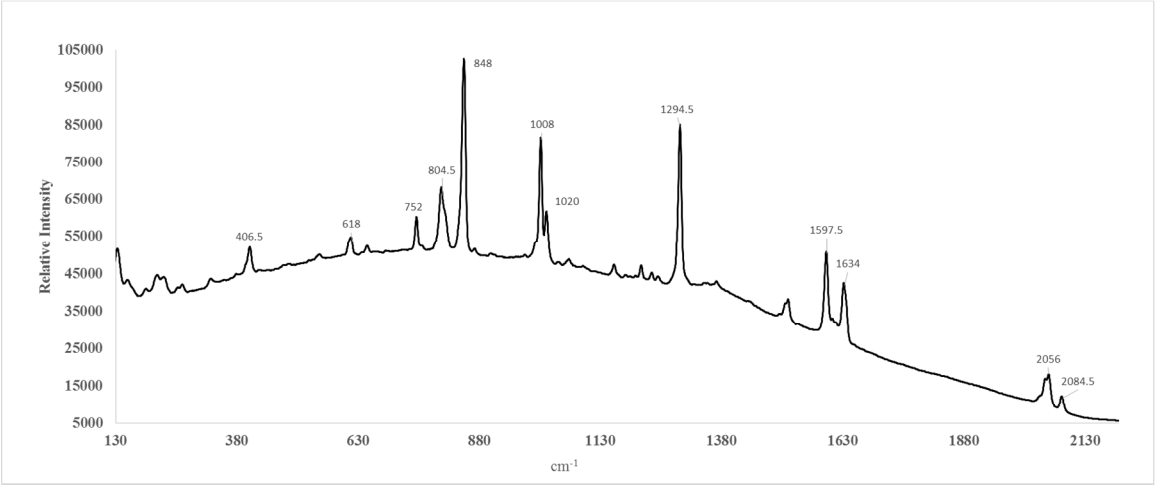

Figures S41. The Raman spectrum of **1**.

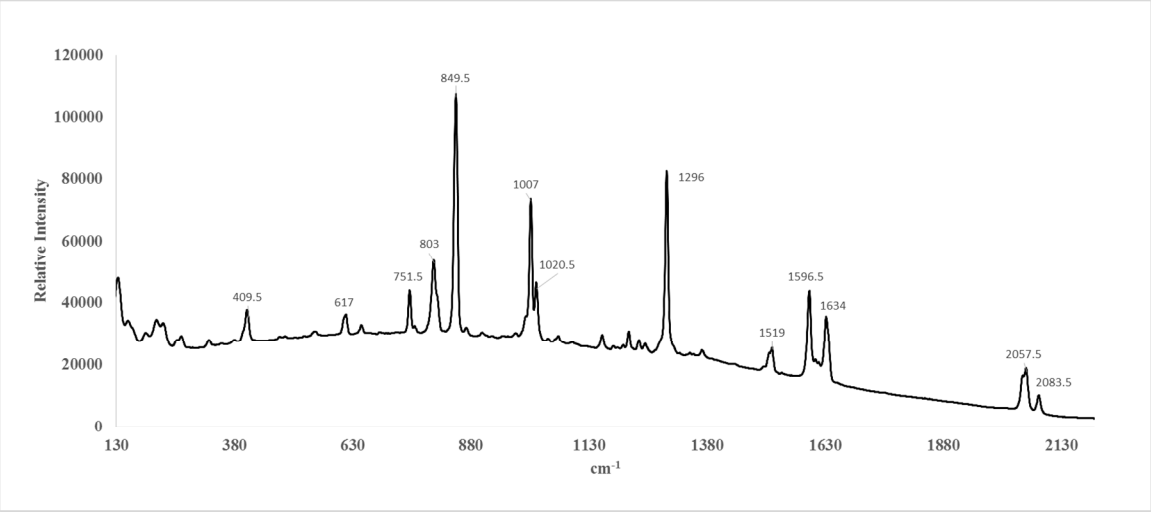

Figure S42. The Raman spectrum of **2**.

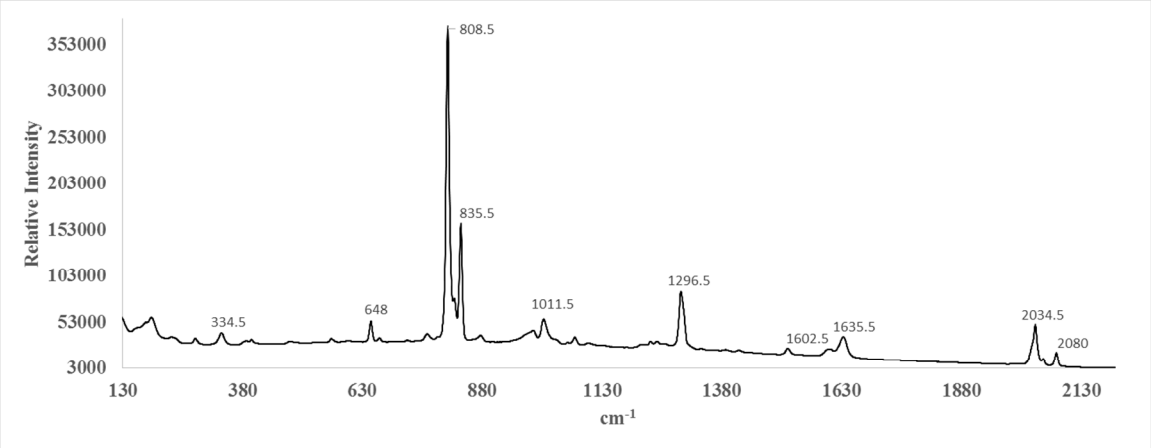

Figure S43. The Raman spectrum of **3**.

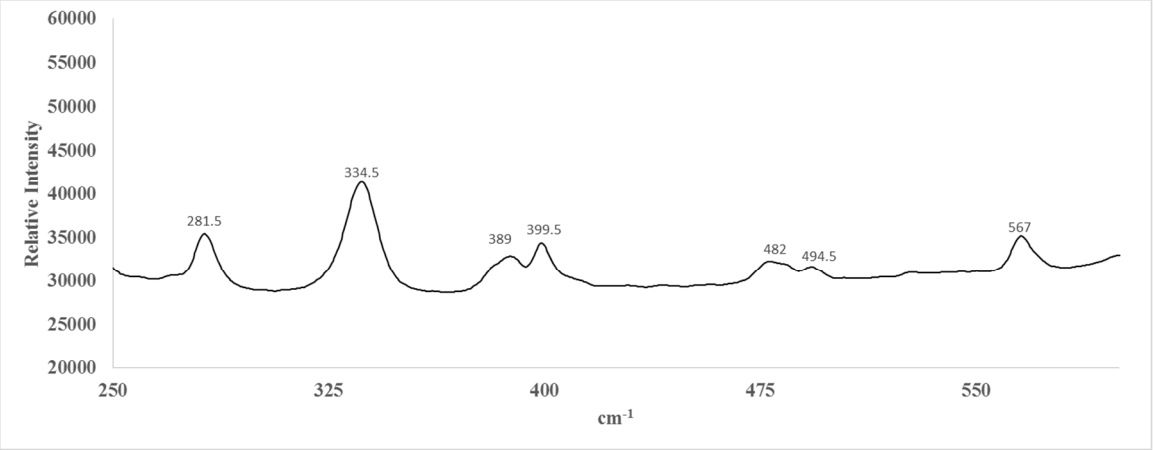

Figure S44. An enlarged view of the Raman spectrum of **3**. Of note are the weak peaks at 482 and 494.5 cm^{-1}, which are attributed to the NCS bending modes.

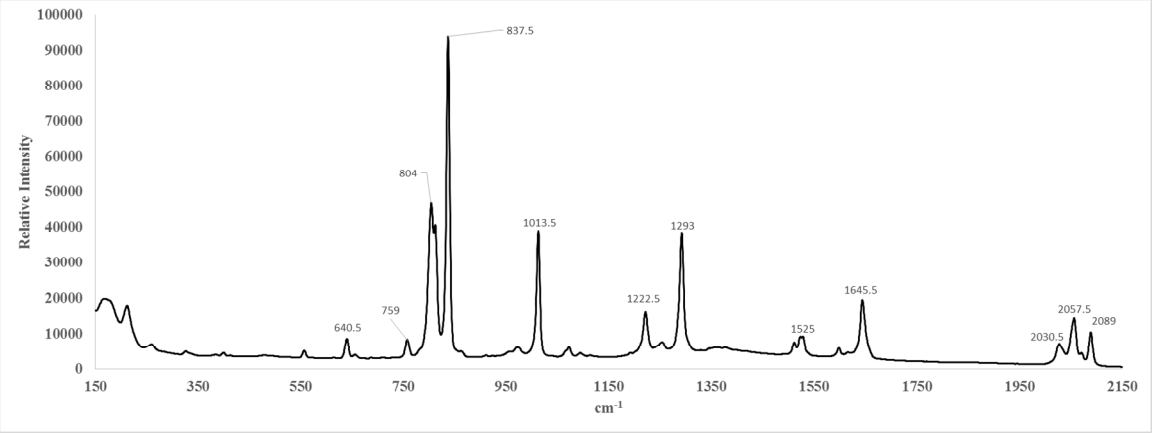

Figure S45. The Raman spectrum of **4**.

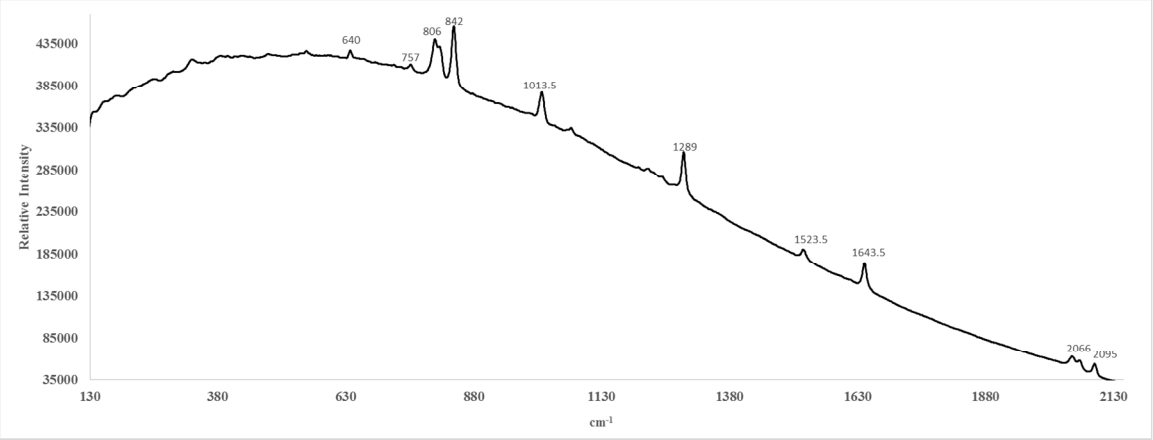

Figure S46. The Raman spectrum of **5**.

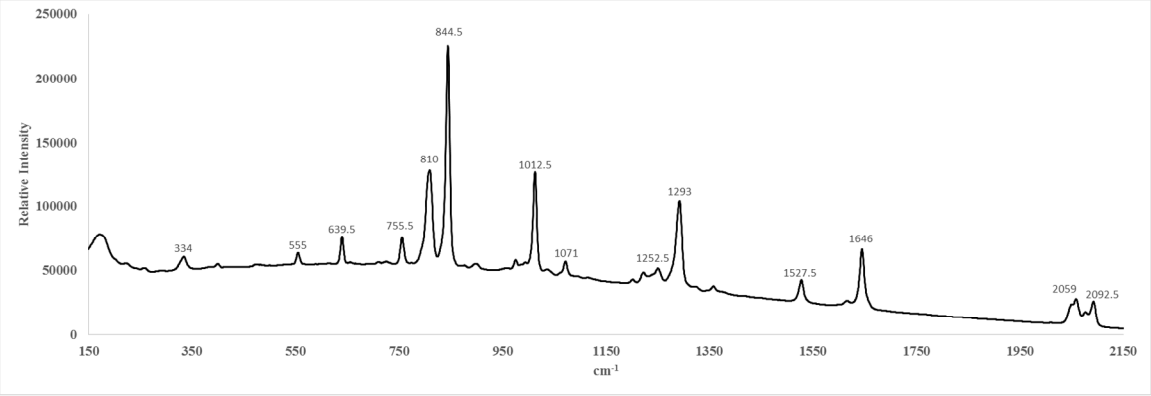

Figure S47. The Raman spectrum of **6**.

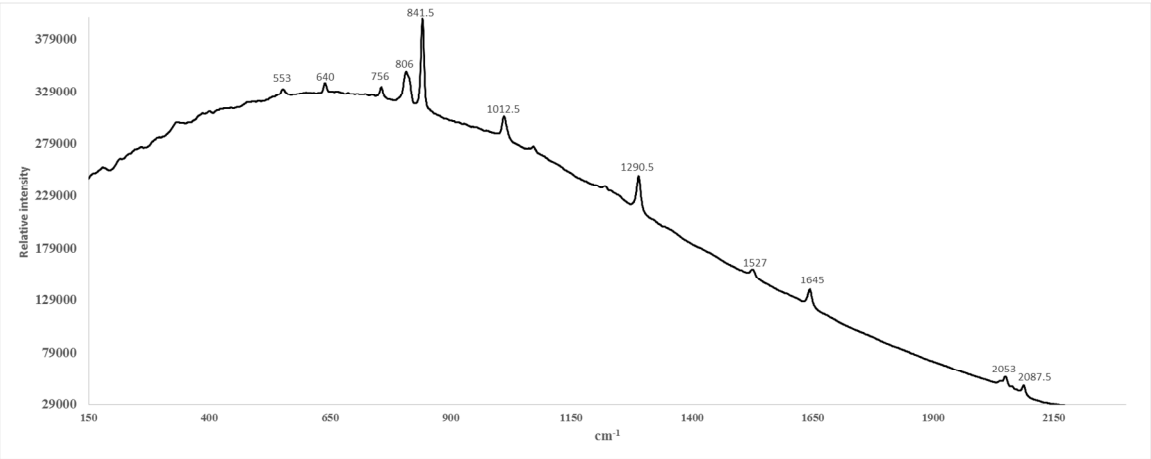

Figure S48. The Raman spectrum of **7**.

12. Thermal ellipsoidal representations of 1 – 7 at 100K and 298K.

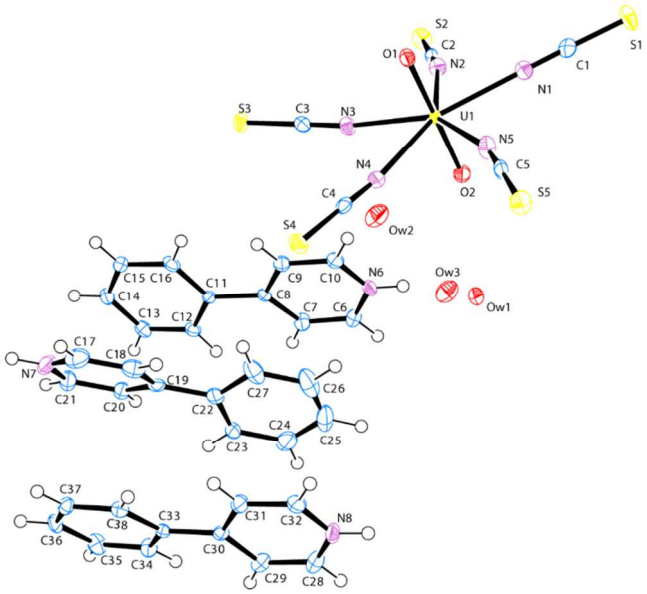

Figure S49. A thermal ellipsoidal representation of **1** at 100K, with thermal ellipsoids shown at the 50% probability level.

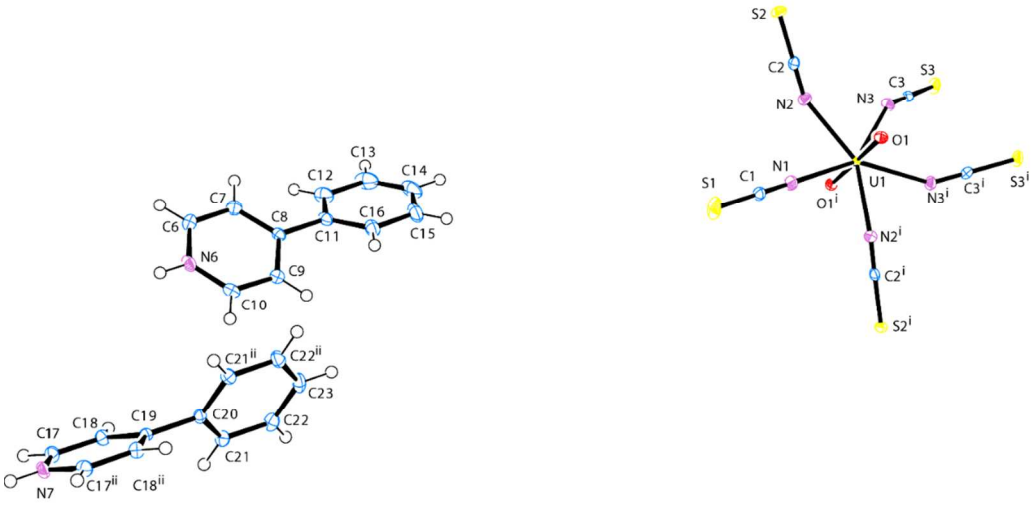

Figure S50. A thermal ellipsoidal representation of **2** at 100K, with thermal ellipsoids shown at the 50% probability level.

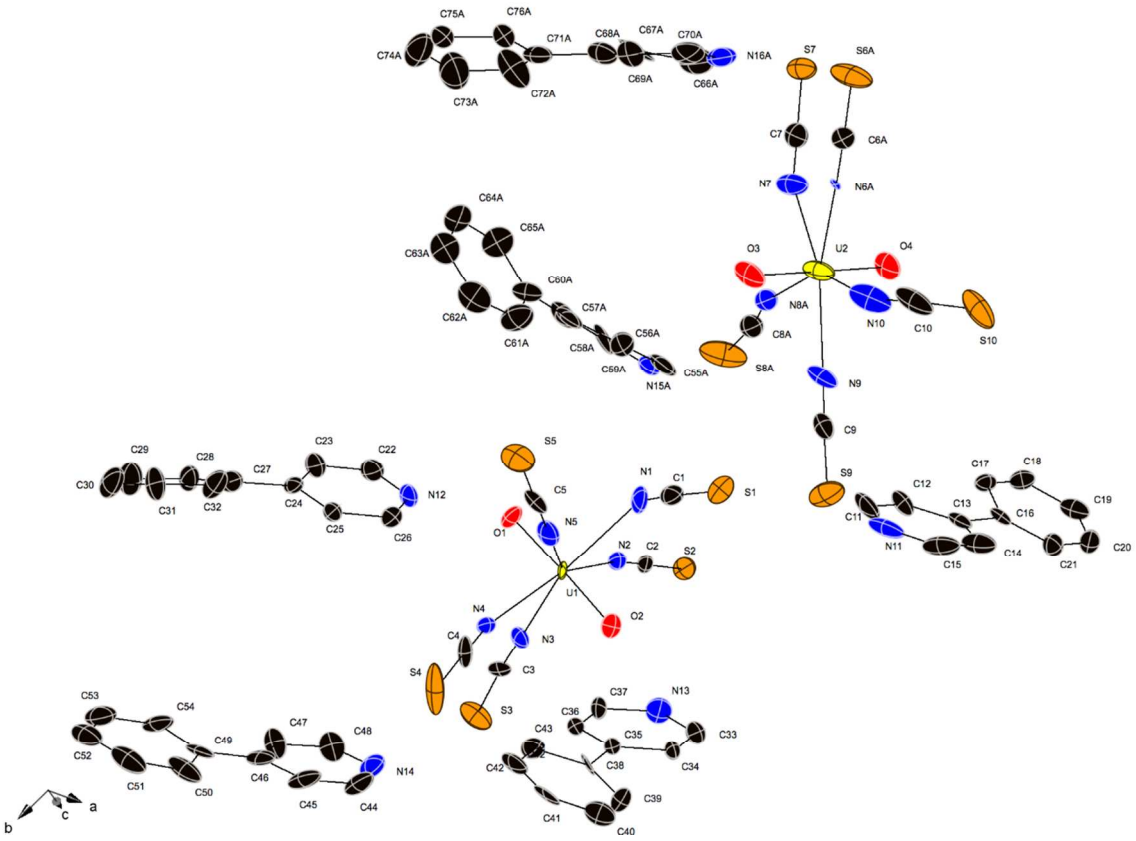

Figure S51. A thermal ellipsoidal representation **1M** at 100K, with thermal ellipsoids shown at the 50% probability level.

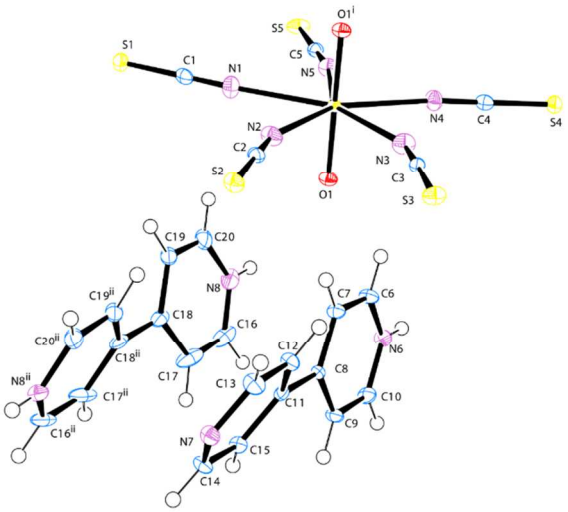

Figure S52. A thermal ellipsoidal representation of **3** at 100K, with thermal ellipsoids shown at the 50% probability level.

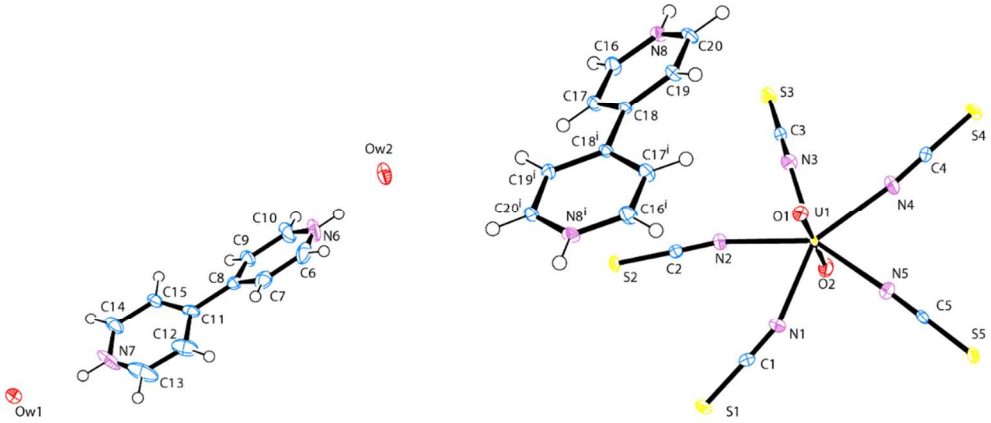

Figure S53. An ORTEP illustration of **4** at 100K, with thermal ellipsoids shown at the 50% probability level.

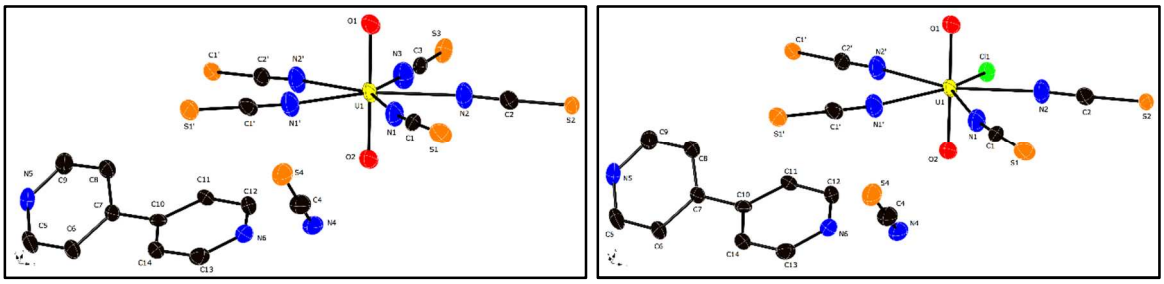

Figure S54. A thermal ellipsoid representation of **5** at 100K, thermal ellipsoids are shown at the 50% probability level, showing both constituents (SCN – **Left** and Cl – **Right**) of the partially occupied ligand site.

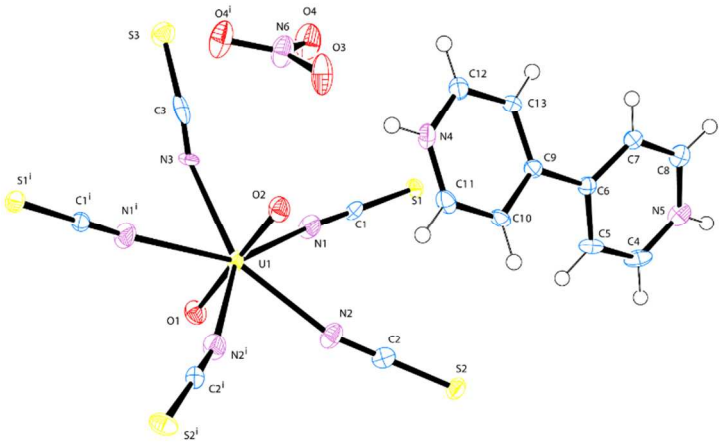

Figure S55. A thermal ellipsoidal of **6** at 100K, with thermal ellipsoids shown at the 50% probability level.

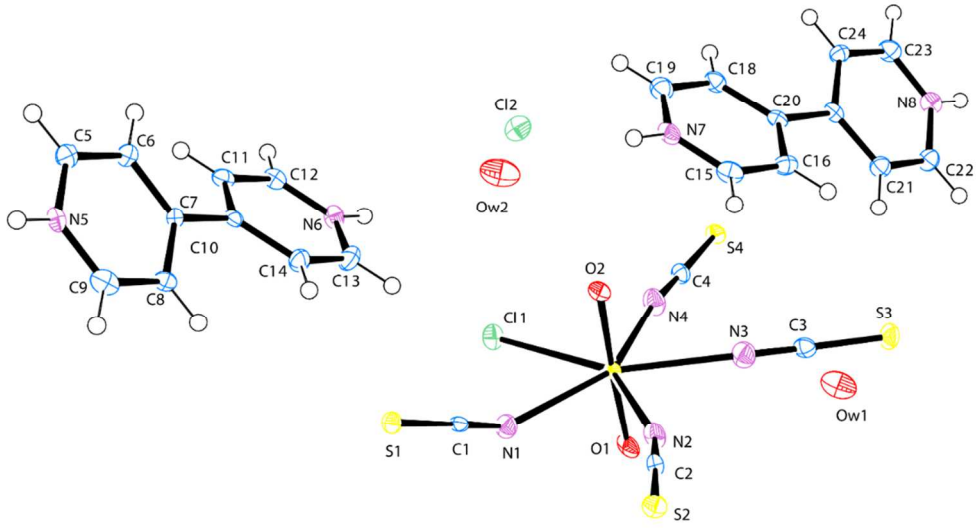

Figure S56. A thermal ellipsoidal representation of **7** at 100K, with thermal ellipsoids shown at the 50% probability level.

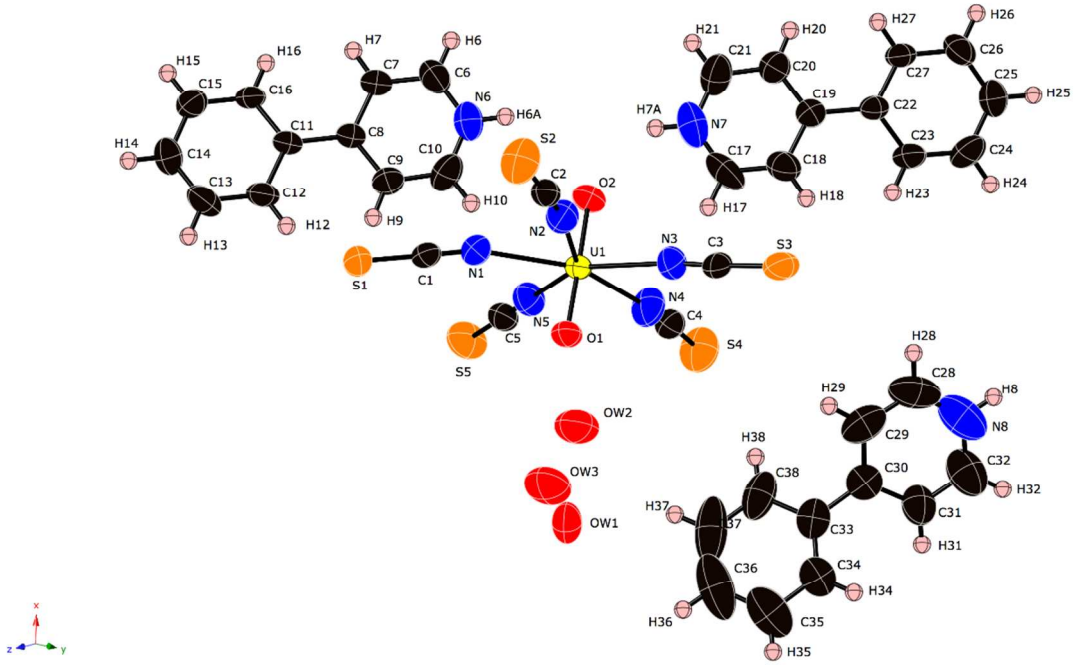

Figure S57. A thermal ellipsoid representation of **1RT** at 285K, with thermal ellipsoids shown at the 50% probability level.

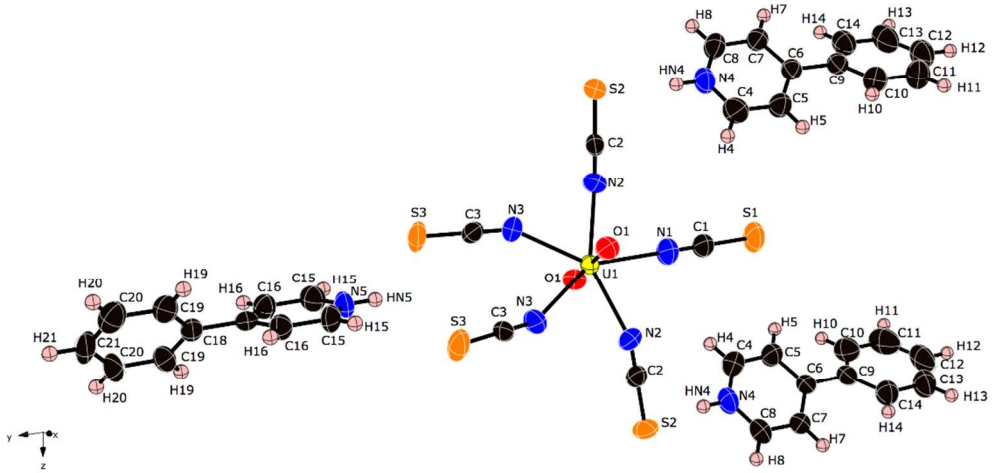

Figure S58. A thermal ellipsoid representation of **2RT** at 296K, with thermal ellipsoids shown at the 50% probability level.

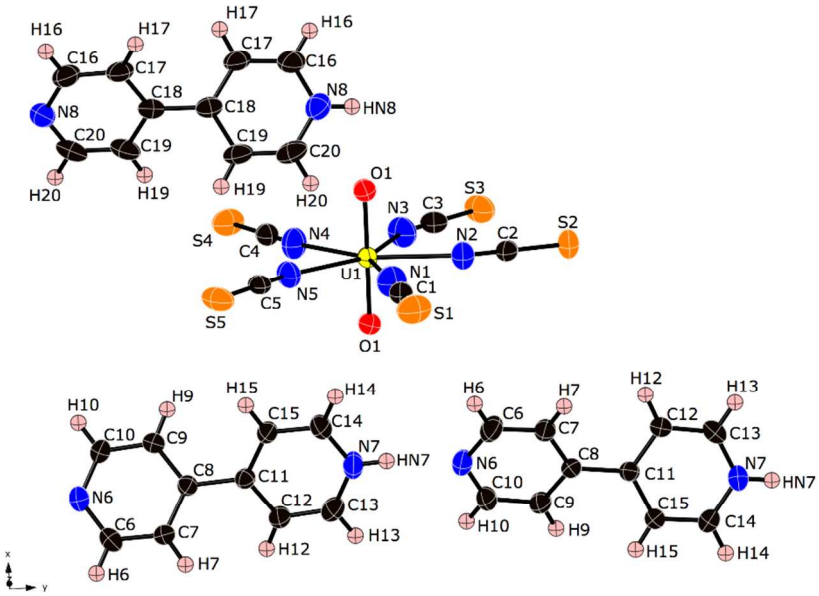

Figure S59. A thermal ellipsoid representation of **3RT** at 296K, with thermal ellipsoids shown at the 50% probability level.

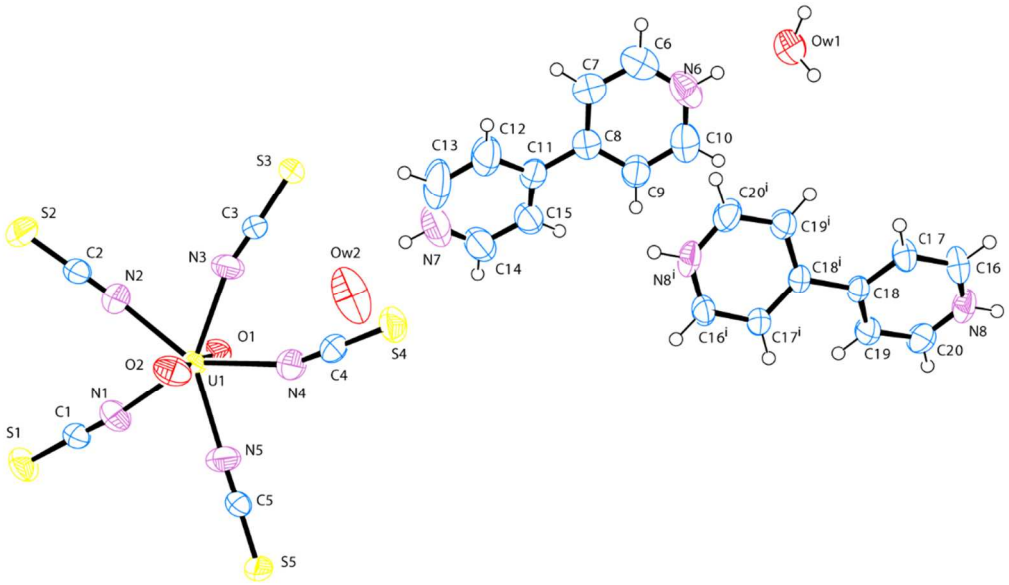

Figure S60. A thermal ellipsoidal representation of **4RT** at 296K, with thermal ellipsoids shown at the 50% probability level.

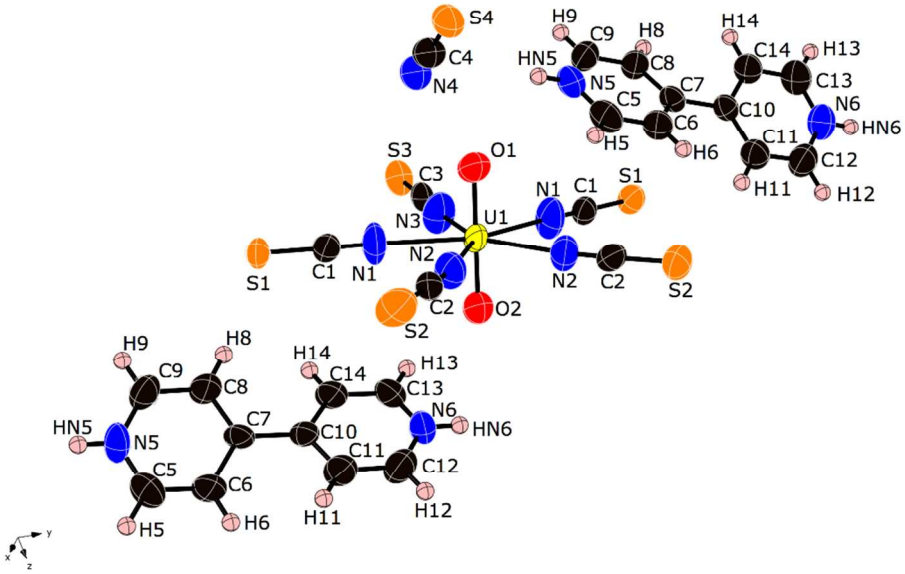

Figure S61. A thermal ellipsoid representation **5RT** at 296K, with thermal ellipsoids shown at the 50% probability level.

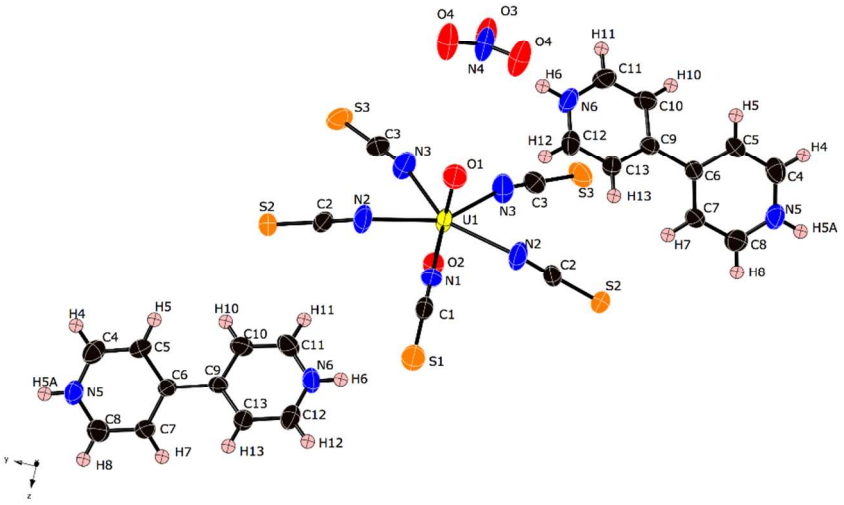

Figure S62. A thermal ellipsoid representation of **6RT** at 296K, with thermal ellipsoids shown at the 50% probability level.

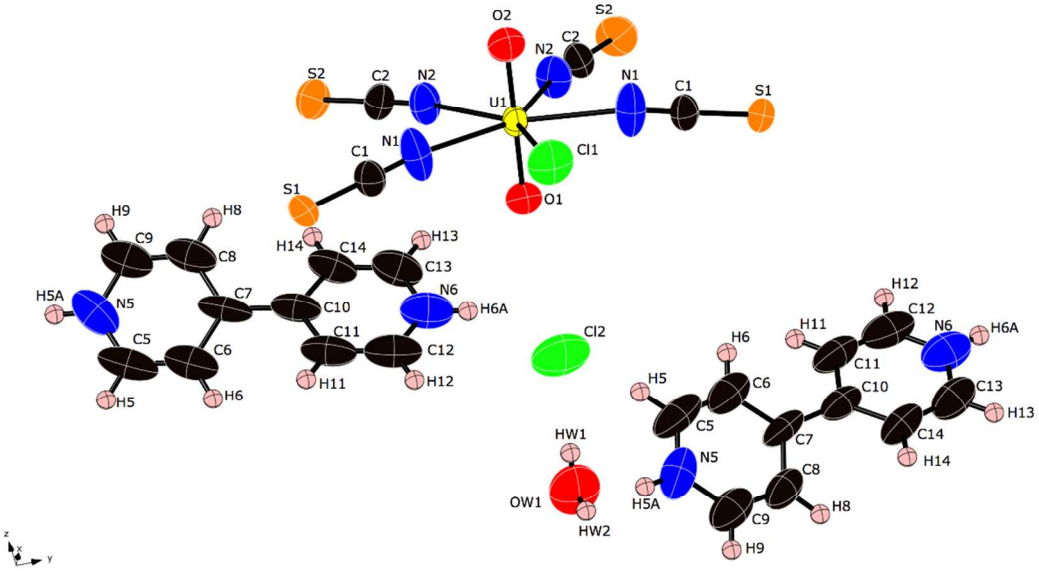

Figure S63. A thermal ellipsoid representation of **7RT** at 296K, with thermal ellipsoids shown at the 50% probability level.

13. References

(1) Cotton, S. In *Lanthanide and Actinide Chemistry*; John Wiley & Sons, Ltd: 2006, p 145.
(2) Mayer, K.; Wallenius, M.; Varga, Z. *Chem. Rev.* 2013, *113*, 884.
(3) GaussView 5.0.9, Roy D. Dennington, Todd A. Keith and John M. Millam, Semichem Inc., 2009
(4) Sheldrick, G. M. *Acta Crystallogr. A* 2008, *64*, 112.
(5) Farrugia, L. *J. Appl. Crystallogr.* 2012, *45*, 849.
(6) Alvarez, S.; Menjón, B.; Falceto, A.; Casanova, D.; Alemany, P. *Inorg. Chem.* 2014, *53*, 12151.
(7) Palmer, D.; Palmer, S. *CrystalMaker V9.2.7* 2016.
(8) Sheldrick, G. M.; 2008/4 ed. Georg-August-Universität Göttingen, Göttingen, Germany., 2008.
(9) Version 3.0 ed.; Bruker Analytical X-ray Systems: Madison, WI, 2013.
(10) Sheldrick, G. M. Univeristy of Göttingen: Göttingen , Germany, 2008.